10
Numerical simulation of baroclinic waves

<u>The role of models in meteorology</u>

In the computer the meteorologist found a most diverting toy. The effort to develop realistic models, first for short-range weather prediction, and more recently for climate simulation and prediction, took precedence over attempts to understand the dynamical nature of the large-scale atmospheric circulation. Since the governing equations are complex and nonlinear, it seemed to many that their numerical solutions would afford the only feasible approach to understanding their implications; and so many of the most ingenious brains in the business devoted themselves to refining numerical schemes and improving the representations of various unresolved but important processes. The deep physical insights into the nature of the atmospheric circulation gained by such men as Rossby and Ertel were all but forgotten by a whole generation of atmospheric scientists. A few academic meteorologists continued to be drawn to the attempt to reduce the atmosphere to its simplest possible essentials, and out of that effort came a deeper appreciation of the way in which nonlinearity manifests itself in the atmosphere. The work of Lorenz and others led to the development of so-called "chaos" theory… This revealed that nonlinearity can act to generate great complexity out of really rather simple equations.
I.N. James (1994), *Introduction to Circulating Atmospheres*. Cambridge University Press. P. xii-xiii.

http://www.staff.science.uu.nl/~delde102/AtmosphericDynamics.htm

10.1 Introduction

With the advent of computers, after the Second World War, a few research centres started investigating the possibility of numerical weather prediction. In 1950 Charney, Fjortoft and von Neuman published a paper, which demonstrated, for the first time, that numerical weather prediction was a feasible project[1]. In the 1950's, Norman Phillips (1956[2]) and others extended this work to climate modelling, by simply running the weather prediction models, with an improved description of diabatic processes, such as radiation, for many model years and studying the model climate, i.e. the statistics of model weather. This led to the emergence of so-called "**General Circulation Models**", for which the acronym, "**GCM**", was introduced. In the 1970's the ocean was included in these models. Nowadays "GCM" stands for "**Global Climate Model**". These models include the atmosphere, oceans, the cryosphere and much more.

From 1980 onwards this line of research developed explosively, together with the required computer power. About 40 global climate/weather prediction models have emerged that are used by a very large community of researchers to study very diverse problems in climate and weather research. Over a time span of many decades several generations of scientists, working at different institutes, contributed to the computer code of these models. Unfortunately, this computer code (usually in FORTRAN) has now become a "black box" to the younger generation of researchers. Too many, especially young climate scientists, under the pressure of managers and politicians, are now using these "comprehensive models" to produce "quick or easy answers", which cannot, or hardly, be verified, to quite superficial questions. They are thus carried away from "fundamental research", which should aim to increase insight and understanding in favour of producing "engineering-results" [3].

This view of the practice and benefit of numerical modelling of weather and climate is, I confess, too pessimistic and, in fact, only applies to "Climate modeling". Impressive progress has been attained with numerical weather prediction models, which, in accordance with correct scientific practice, are tested every day against observations [4]. The following three chapters intend to demonstrate how numerical models can also be of great value in basic research, if used intelligently, for instance in the form a hierarchy of models of increasing complexity, as suggested by Held (2005) (quoted at the beginning of chapter 8).

A numerical model which aims to predict the weather down to horizontal scales of 10 km or less will have to be based on a rather complete set of equations, including a detailed description of the local forcing, such as variations in terrain, condensation heating and evaporative cooling, emission, transfer and absorption of long-wave and short-wave radiation, conduction of heat at the earth-air interface and upward turbulent transfer of heat, momentum and moisture in the boundary layer (**figure 10.1**). This, obviously, is a very extensive and difficult task.

Neglecting, for the moment, the fact that there is intrinsic unpredictibility in a nonlinear system like the atmosphere [5], we may state that predictability of weather is determined

---

[1] Charney, J.G., R. Fjortoft and J. von Neumann, 1950: Numerical Integrtation of the barotropic Vortcity Equation. **Tellus, 2**, 237-254.

[2] Phillips, N.A., 1956: The general circulation of the atmosphere: a numerical experiment. **Q.J.Roy.Meteorol.Soc., 82**, 123-164.

[3] Meehl, Gerald A., and Coauthors, 2009: Decadal Prediction. Can it be skillful? **Bull. Amer. Meteor. Soc., 90**, 1467–1485.

[4] Bauer, P., A. Thorpe and G. Brunet, 2015: The quiet revolution of numerical weather prediction. **Nature 525**, 47-55.

[5] E.N. Lorenz, 1963: Deterministic nonperiodic flow. **J.Atmos.Sci., 20**, 130-141.

principally by **(a)** knowledge of the initial conditions, **(b)** knowledge of the boundary conditions in space, and **(c)** representation of "forcing" in the model.

The **<u>initial condition</u>** is obtained from a combination of observations, a model prediction from a previous state (e.g. six hours earlier), which represents a first guess, and the requirement that the velocity field and the pressure field are in some kind of dynamic balance (e.g. geostrophic balance). This last requirement is imposed in order to prevent as much as possible the excitation of waves in the model from imbalances due to observation errors. However, there is the danger that this condition also filters out real imbalances that are essential for the (further) development of certain weather systems. Another problem with the **<u>balance condition</u>** is that the equations describing the balanced state must be of the elliptic type. Only then can a unique initial state be found. The potential vorticity inversion equation, which is dicussed at length in chapter 7, is an example of such an equation.
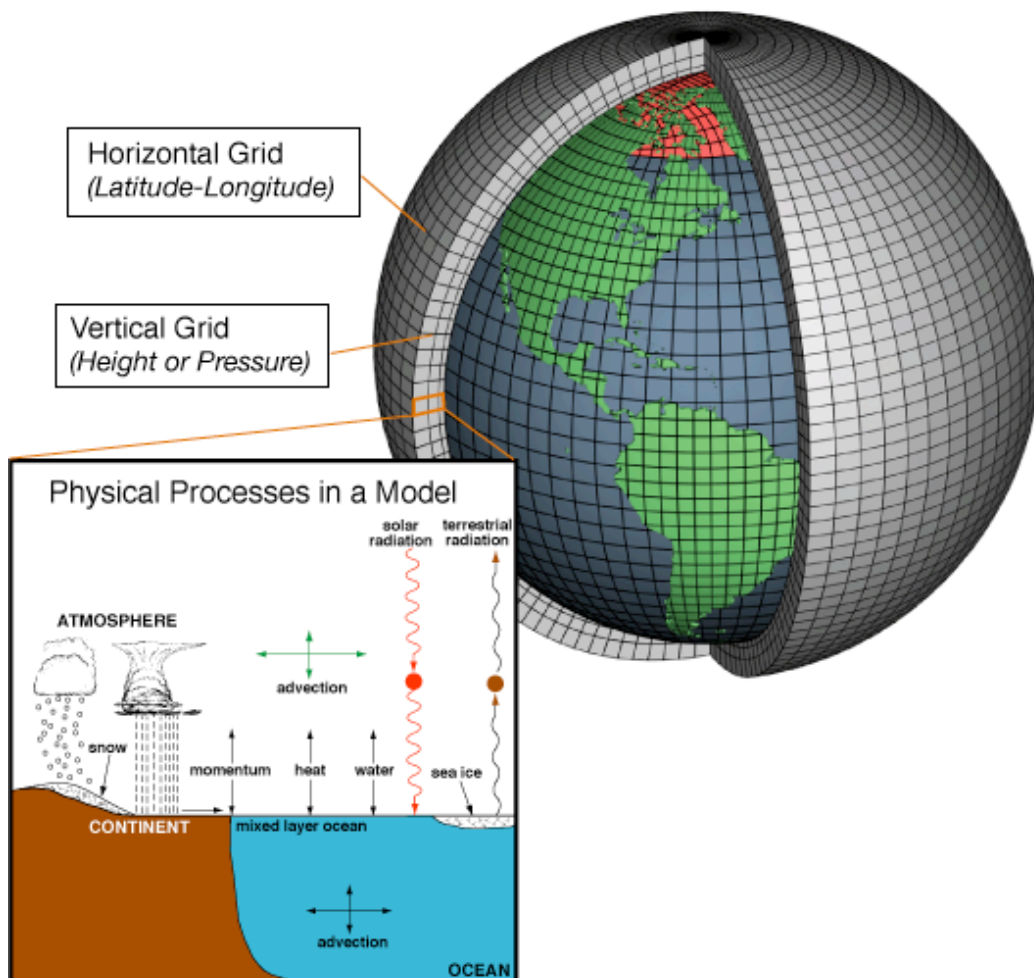

FIGURE 10.1. A climate model is based on the differential equations describing the budgets of mass, energy and momentum in the oceans and atmosphere, together with the appropriate equations of state. The domain of a climate model is divided into a 3-dimensional grid. Numerical approximations of the equations are formulated for each grid point. Note that we are confronted with a problem at the pole due to the convergence of the meridians. This so-called "**<u>pole problem</u>**" is discussed in interesting paper by D.L. Williamson in the list of references to this chapter). Source of the figure: https://en.wikipedia.org/wiki/General_Circulation_Model.
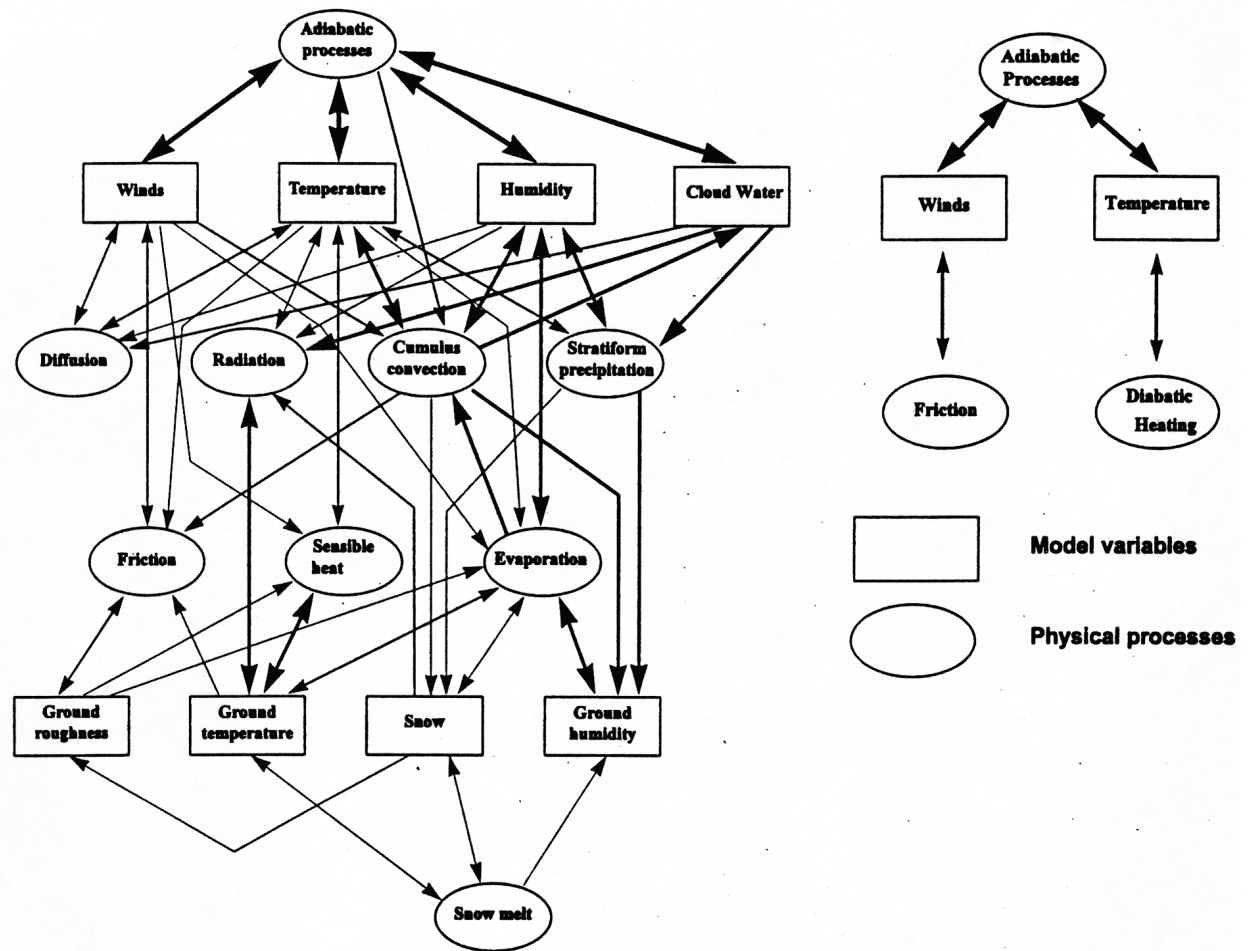
FIGURE 10.2. Processes in a normal weather prediction model or full general circulation model (GCM) (left); processes in the "dynamical core" of a primitive equation model (right).

The principal **measurements** that are used to initialize a model are measurements of vertical profiles of wind, temperature and moisture. At first sight, the spatial and the temporal resolution as well as the accuracy of the present upper air observation system (radiosondes, satellites, radar-networks and other ground-based remote sensing installations) hardly seems adequate for numerical weather forecasting. Nevertheless, numerical models seem to perform surprisingly well in forecasting the weather a few days ahead. This indicates that the expected errors in the initial state are usually and fortunately not detrimental. Probably this is due to the fundamental fact that the dynamics of the atmosphere at all scales is **slaved to the *large scale* potential vorticity distribution** (chapter 7).

In 2006 the IFS model of ECMWF [6], which is based on the same equations as the model described in this chapter, had a resolution of about 25 km. The 2006 version of the model is, therefore, able to resolve circulations with horizontal scales larger than 50 km. There are 91 levels between the Earth's surface and 80 km above sea level. There are 76,757,590 grid points in the upper air and 3,373,960 grid points in surface and sub-surface layers. The domain covers the whole globe and, therefore, does not need the specification of lateral boundary conditions[7].

---

[6] ECMWF: European Centre for Medium Range Weather Forecasts. See http://www.ecmwf.int/research/

[7] The 2016 version of IFS has a resolution of 16 km and 137 vertical levels .

The current generation of numerical weather prediction models, used for short range (6 to 36 hours) high-resolution weather prediction, cover a "limited area", for instance Western Europe and the adjacent Atlantic Ocean. Therefore, **lateral boundary conditions** are required for these models. These boundary conditions are obtained from the output of a numerical model with a lower resolution covering a larger area (e.g. the global IFS model of ECMWF). A study performed by Anthes et al. (1989)[8] has shown that the lateral boundary condition is the most important factor determining the skill of a limited area model for forecast-periods up to 36 hours. This also demonstrates that large-scale motions have a major, if not dominant, effect on the evolution of the smaller scale (i.e. meso-scale) motions.

The representation of the **diabatic forcing**, such as absorption of radiation, depends on our theoretical knowledge of the physical processes responsible for the forcing. Finding a good representation of the forcing, especially when this forcing is operating on a relatively small scale (such as the process of evaporation at the Earth's surface or latent heat release in clouds), is probably the most difficult aspect of numerical modelling of atmospheric circulations. For example, for the simulation and prediction of the formation of a tropical cyclone the representation of the forcing due to latent heat release is of crucial importance. The evolution and, therefore, the predictability of fog depends strongly on the longwave radiative cooling at top of the fog layer, the shortwave radiative warming of the fog by absorption and the penetration of Solar radiation through "holes" in the fog layer, which can then lead to warming of the boundary layer from below. The formation of thunderstorms, on the other hand, depends very strongly on moisture flux convergence (chapter 4), which, in turn is determined by the lower boundary conditions, i.e. the the moisture content and other properties of the **lower boundary** (the earth's surface).
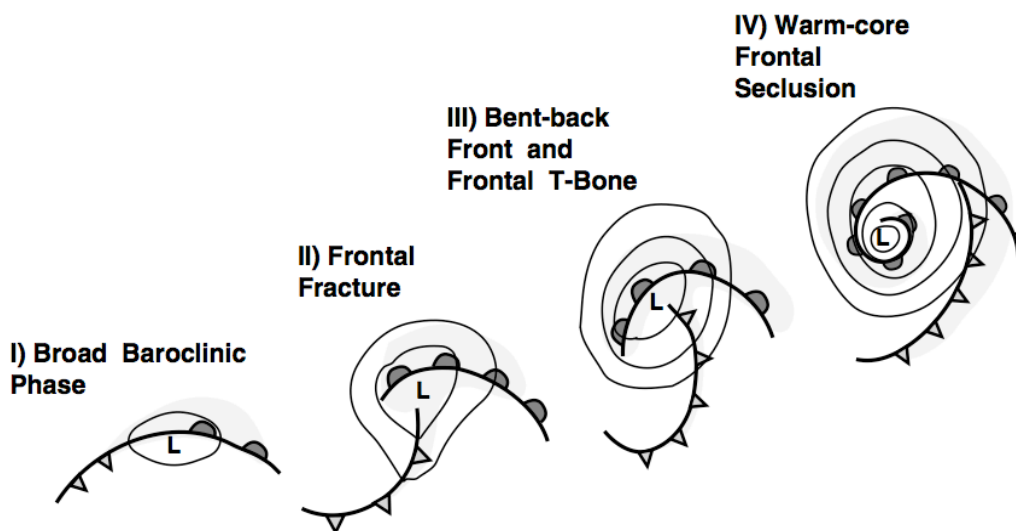

FIGURE 10.3. Conceptual model, proposed by Shapiro and Keyser in 1990, but strongly inspired on work originating in a classical publication due to the "Bergen School of Meteorology" (Bjerknes, J., 1919: On the structure of moving cyclones. **Mon.Wea.Rev., 47**, 95-99), of four stages in the life-cycle of an unstable baroclinic wave (frontal cyclone evolution), over a period of the order of 3 days. Source of this figure: A.T. Semple, 2003: A review and unification of conceptual models of cyclogenesis. **Meteorol.Appl.**, **10**, 39-59.

---

[8]Anthes, R.A., Y-H Kuo, E-Y Hsie, S. Low-Nam and T.W. Bettge, 1989: Estimation of skill and uncertainty in regional numerical models. **Q.J.R.Meteorol.Soc.**, 115, 763-806.

In the following a detailed description is given of an adiabatic numerical model of the atmosphere. Apart from having simplified boundary conditions, the physical content of this model is very similar to the adiabatic physical content, i.e. the **dynamical core**, of present day weather prediction model (**figure 10.2**). This chapter shows how the dynamical core of a primitive equation model can be used to study the **life-cycle of an adiabatic unstable baroclinic wave** (**figure 10.3**). This has become a **classical problem in numerical modeling of atmospheric dynamics**. We will discover that the adiabatic dynamical core of a primitive equation model is able to reproduce the observed life-cycle of a middle latitude cyclone, a so-called "**baroclinic life-cycle**", over a period of 3-5 days, as illustrated in **figure 10.3**, very faithfully. This simulation will serve as an illustration of the theory of **wave-zonal mean flow interaction**, which is presented in **chapter 11**.

In **chapter 12** we will add parametrisations of diabatic processes (**"diabatic" forcing**), associated with radiation and the water cycle, to this model, so that we are equipped to study the large-scale adjustment of the atmosphere to seasonal changes in radiative fluxes and to changes in the intensity of the hydrological cycle.

10.2 Primitive equations

If we assume that motions in the atmosphere are hydrostatic, the governing equations can be written with pressure as a vertical coordinate. The resulting system then consists of three prognostic equations (the x- and y-components of the momentum equation and the thermodynamic energy equation) and three diagnostic equations (the continuity equation, the hydrostatic equation, and the equation of state), constituting a closed system of equations referred to as the **primitive equations**. With pressure as a vertical coordinate these equations are (**Box 9.1**).

$$\frac{du}{dt} - fv = -\left[\frac{\partial \Phi}{\partial x}\right]_p , \tag{10.1}$$

$$\frac{dv}{dt} + fv = -\left[\frac{\partial \Phi}{\partial y}\right]_p , \tag{10.2}$$

$$\frac{\partial \Phi}{\partial p} = -\alpha , \tag{10.3}$$

$$\frac{d\theta}{dt} = \frac{J}{\Pi} , \tag{10.4}$$

$$\left[\frac{\partial u}{\partial x} + \frac{\partial v}{\partial y}\right]_p + \frac{\partial \omega}{\partial p} = 0 . \tag{10.5}$$

The unknown variables are the horizontal velocity, $\vec{v}$, the vertical velocity, ω, the geopotential, Φ, and the potential temperature, θ. The specific volume, α, can be expressed in terms of the potential temperature, θ, using the ideal gas law and the definition of the potential temperature.

If we want to describe large scale circulations accurately, especially at high latitudes we must take the sphericity of the Earth's surface into account. In a spherical form, appropriate to the Earth's non-planar surface, the primitive equations are slightly more complex. The three directions are then: longitude (λ), latitude (ϕ) and radial distance (r) measured from the Earth's centre. The velocity components in terms of these coordinates are,

$$u = r\cos\phi\frac{d\lambda}{dt} \approx a\cos\phi\frac{d\lambda}{dt}; v = r\frac{d\phi}{dt} \approx a\frac{d\phi}{dt}; w = \frac{dr}{dt}. \tag{10.6}$$

The primitive equations in this curved coordinate system, again with pressure as a vertical coordinate are

$$\frac{du}{dt} - \left(f + \frac{u\tan\phi}{a}\right)v = -\frac{1}{a\cos\phi}\left[\frac{\partial\Phi}{\partial\lambda}\right]_p = -\left[\frac{\partial\Phi}{\partial x}\right]_p, \tag{10.7}$$

$$\frac{dv}{dt} + \left(f + \frac{u\tan\phi}{a}\right)u = -\frac{1}{a}\left[\frac{\partial\Phi}{\partial\phi}\right]_p = -\left[\frac{\partial\Phi}{\partial y}\right]_p, \tag{10.8}$$

$$\frac{\partial\Phi}{\partial p} = -\alpha, \tag{10.9}$$

$$\frac{d\theta}{dt} = \frac{J}{\Pi}, \tag{10.10}$$

$$\frac{1}{a\cos\phi}\left(\frac{\partial u}{\partial\lambda} + \frac{\partial(v\cos\phi)}{\partial\phi}\right)_p + \frac{\partial\omega}{\partial p} = 0. \tag{10.11}$$

The material derivative in the spherical coordinate system is written as ($r \approx a = 6370$ km)

$$\frac{d}{dt} = \frac{\partial}{\partial t} + \frac{u}{a\cos\phi}\left[\frac{\partial}{\partial\lambda}\right]_p + \frac{v}{a}\left[\frac{\partial}{\partial\phi}\right]_p + \omega\frac{\partial}{\partial p}, \tag{10.12}$$

which is the same as

$$\frac{d}{dt} = \frac{\partial}{\partial t} + u\left[\frac{\partial}{\partial x}\right]_p + v\left[\frac{\partial}{\partial y}\right]_p + \omega\frac{\partial}{\partial p}. \tag{10.13}$$

10.3 The sigma coordinate system

The (x, y, p, t) coordinate system possesses certain advantages over the (x, y, z, t) system, relating to the simplification of the primitive equations. However, the task of imposing the lower boundary condition is not easy. A solution to this problem was first proposed by Norman Phillips was the first to propose the so-called "**sigma-coordinate**" system, which greatly simplifies this task. In the sigma-coordinate system the vertical coordinate is not pressure, but pressure normalized by the pressure at the earth's surface (p_s), i.e.

$$\boxed{\sigma \equiv \frac{p}{p_s}}. \tag{10.14}$$

Therefore, σ is nondimensional. The lower boundary condition, i.e. at the earth's surface, is $\sigma=1$ and $d\sigma/dt=0$, even with varying height of the earth's surface.

We must now transform the set of equations (10.7-11) to σ-coordinates. **Figure 10.4** sketches the problem at hand. The gradient of the geopotential on a surface of constant pressure needs to be expressed as a gradient of the geopotential on a surface of constant σ.
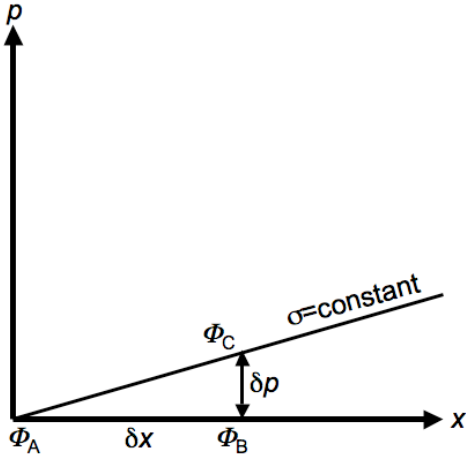
FIGURE 10.4. Illustrating the transformation of the geopotential gradient from the pressure coordinate to the sigma-coordinate (see text).

We can write,

$$\frac{\Phi_C - \Phi_A}{\delta x} = \frac{\Phi_C - \Phi_B}{\delta p}\frac{\delta p}{\delta x} + \frac{\Phi_B - \Phi_A}{\delta x}.$$

Assuming that $\delta x \Rightarrow 0$ and $\delta p \Rightarrow 0$ we obtain

$$\left(\frac{\partial \Phi}{\partial x}\right)_\sigma = \left(\frac{\partial \Phi}{\partial p}\right)\left(\frac{\partial p}{\partial x}\right)_\sigma + \left(\frac{\partial \Phi}{\partial x}\right)_p.$$

This can be rewritten as follows.

$$\left(\frac{\partial \Phi}{\partial x}\right)_\sigma = \left(\frac{\partial \Phi}{\partial p}\right)\left(\frac{\partial p}{\partial x}\right)_\sigma + \left(\frac{\partial \Phi}{\partial x}\right)_p = \left(\frac{\partial \sigma}{\partial p}\right)\left(\frac{\partial \Phi}{\partial \sigma}\right)\left(\frac{\partial p}{\partial x}\right)_\sigma + \left(\frac{\partial \Phi}{\partial x}\right)_p = \frac{1}{p_s}\left(\frac{\partial \Phi}{\partial \sigma}\right)\sigma\frac{\partial p_s}{\partial x} + \left(\frac{\partial \Phi}{\partial x}\right)_p$$

$$= \sigma\left(\frac{\partial \Phi}{\partial \sigma}\right)\frac{\partial \ln p_s}{\partial x} + \left(\frac{\partial \Phi}{\partial x}\right)_p$$

With this, the two horizontal components of the momentum equations with σ as vertical coordinate becomes

$$\frac{du}{dt} - \left(f + \frac{u\tan\phi}{a}\right)v = -\left[\frac{\partial \Phi}{\partial x}\right]_\sigma + \frac{\sigma}{p_s}\frac{\partial p_s}{\partial x}\frac{\partial \Phi}{\partial \sigma}, \tag{10.15}$$

$$\frac{dv}{dt} + \left(f + \frac{u\tan\phi}{a}\right)u = -\left[\frac{\partial \Phi}{\partial y}\right]_\sigma + \frac{\sigma}{p_s}\frac{\partial p_s}{\partial y}\frac{\partial \Phi}{\partial \sigma}, \tag{10.16}$$

where the total derivative is

$$\frac{d}{dt} = \frac{\partial}{\partial t} + \frac{u}{a\cos\phi}\left[\frac{\partial}{\partial\lambda}\right]_\sigma + \frac{v}{a}\left[\frac{\partial}{\partial\phi}\right]_\sigma + \frac{d\sigma}{dt}\frac{\partial}{\partial\sigma} \ . \tag{10.17}$$

The equation of continuity can be transformed by writing the horizontal divergence as

$$\frac{1}{a\cos\phi}\left(\frac{\partial u}{\partial\lambda} + \frac{\partial(v\cos\phi)}{\partial\phi}\right)_p = \frac{1}{a\cos\phi}\left\{\left(\frac{\partial u}{\partial\lambda} + \frac{\partial(v\cos\phi)}{\partial\phi}\right)_\sigma - \frac{1}{p_s}\frac{\partial p}{\partial\lambda}\frac{\partial u}{\partial\sigma} - \frac{1}{p_s}\frac{\partial p}{\partial\phi}\frac{\partial v\cos\phi}{\partial\sigma}\right\} \tag{10.18}$$

To transform the term $\partial\omega/\partial p$ we note first that

$$\frac{\partial}{\partial p} = \frac{\partial}{\partial\sigma p_s} = \frac{1}{p_s}\frac{\partial}{\partial\sigma} \ . \tag{10.19}$$

Therefore, the continuity equation can be written as

$$\frac{1}{a\cos\phi}\left\{\left(\frac{\partial u}{\partial\lambda} + \frac{\partial(v\cos\phi)}{\partial\phi}\right)_\sigma - \frac{1}{p_s}\frac{\partial p}{\partial\lambda}\frac{\partial u}{\partial\sigma} - \frac{1}{p_s}\frac{\partial p}{\partial\phi}\frac{\partial v\cos\phi}{\partial\sigma}\right\} + \frac{1}{p_s}\frac{\partial\omega}{\partial\sigma} = 0. \tag{10.20}$$

The "vertical velocity" in the sigma coordinate system is

$$\frac{d\sigma}{dt} = \frac{d}{dt}\left(\frac{p}{p_s}\right) = \frac{1}{p_s}\frac{dp}{dt} - \frac{p}{p_s^2}\frac{dp_s}{dt} = \frac{\omega}{p_s} - \frac{\sigma}{p_s}\frac{dp_s}{dt} = \frac{\omega}{p_s} - \frac{\sigma}{p_s}\left(\frac{\partial p_s}{\partial t} + \vec{v}\cdot\vec{\nabla}p_s\right). \tag{10.21}$$

Differentiating this equation with respect to σ yields

$$\frac{\partial}{\partial\sigma}\frac{d\sigma}{dt} = -\left(\frac{\partial p_s}{\partial t} + \vec{v}\cdot\vec{\nabla}p_s\right)\frac{\partial}{\partial\sigma}\left(\frac{\sigma}{p_s}\right) - \left(\frac{\sigma}{p_s}\right)\frac{\partial}{\partial\sigma}\left(\frac{\partial p_s}{\partial t} + \vec{v}\cdot\vec{\nabla}p_s\right) + \frac{\partial}{\partial\sigma}\left(\frac{\omega}{p_s}\right)$$

or

$$p_s\frac{\partial}{\partial\sigma}\frac{d\sigma}{dt} = -\left(\frac{\partial p_s}{\partial t} + \vec{v}\cdot\vec{\nabla}p_s\right) - \sigma\frac{\partial}{\partial\sigma}\left(\vec{v}\cdot\vec{\nabla}p_s\right) + \frac{\partial\omega}{\partial\sigma}$$

Using (10.18) and (10.20) we obtain the definitive form of the **continuity equation**:

$$\boxed{\frac{\partial p_s}{\partial t} + \frac{1}{a\cos\phi}\left(\frac{\partial p_s u}{\partial\lambda} + \frac{\partial(p_s v\cos\phi)}{\partial\phi}\right) + p_s\frac{\partial}{\partial\sigma}\left(\frac{d\sigma}{dt}\right) = 0} \ . \tag{10.22}$$

The **hydrostatic equation**, with σ as vertical coordinate, may be written as

$$\boxed{\frac{\partial\Phi}{\partial\sigma} = -\frac{RT}{\sigma} = -\frac{R\theta}{\sigma}\left(\frac{p}{p_{ref}}\right)^{R/c_p}} \tag{10.23}$$

where we have made use of the equation of state, and the definition of potential temperature, θ. The potential temperature equation may be written as

$$\frac{\partial \theta}{\partial t} + \frac{u}{a\cos\phi}\left[\frac{\partial \theta}{\partial \lambda}\right]_\sigma + \frac{v}{a}\left[\frac{\partial \theta}{\partial \phi}\right]_\sigma + \frac{d\sigma}{dt}\frac{\partial \theta}{\partial \sigma} = \frac{J}{\Pi} \tag{10.24}$$

If we now multiply the continuity equation (10.22) by θ, multiply (10.24) by p_s, and add the two resulting equations we get **flux form of the potential temperature equation** (in σ-coordinates) [9]:

$$\frac{\partial p_s\theta}{\partial t} = -\frac{1}{a\cos\phi}\left(\frac{\partial p_s u\theta}{\partial \lambda} + \frac{\partial p_s v\theta\cos\phi}{\partial \phi}\right) - \frac{\partial}{\partial \sigma}\left(p_s\theta\frac{d\sigma}{dt}\right) + \frac{p_s J}{\Pi} \quad,$$

which can also be written as

$$\boxed{\frac{\partial p_s\theta}{\partial t} = \frac{p_s v\theta}{a}\tan\phi - \left(\frac{\partial p_s u\theta}{\partial x} + \frac{\partial p_s v\theta}{\partial y}\right) - \frac{\partial}{\partial \sigma}\left(p_s\theta\frac{d\sigma}{dt}\right) + \frac{p_s J}{\Pi}} \tag{10.25}$$

An analogous transformation of the **momentum equations** (10.7-8) to σ-coordinates yields

$$\boxed{\frac{\partial p_s u}{\partial t} = -\left(\frac{\partial p_s u^2}{\partial x} + \frac{\partial p_s uv}{\partial y}\right) - \frac{\partial}{\partial \sigma}\left(p_s u\frac{d\sigma}{dt}\right) + \left(f + \frac{2u\tan\phi}{a}\right)p_s v - \frac{1}{a\cos\phi}\left(p_s\frac{\partial \Phi}{\partial \lambda} + RT\frac{\partial p_s}{\partial \lambda}\right)}$$
$$\tag{10.26}$$

$$\boxed{\frac{\partial p_s v}{\partial t} = -\left(\frac{\partial p_s uv}{\partial x} + \frac{\partial p_s v^2}{\partial y}\right) - \frac{\partial}{\partial \sigma}\left(p_s u\frac{d\sigma}{dt}\right) - \left(f + \frac{u\tan\phi}{a}\right)p_s u + \frac{p_s v^2}{a}\tan\phi - \frac{1}{a}\left(p_s\frac{\partial \Phi}{\partial \phi} + RT\frac{\partial p_s}{\partial \phi}\right)}$$
$$\tag{10.27}$$

The set of equations (10.22), (10.23), (10.25), (10.26) and (10.27) contains the six independent variables u, v, $d\sigma/dt$, θ, Φ and p_s. Therefore, we need an additional equation to make this set solvable. This additional equation is obtained by integrating the continuity equation (10.22) vertically and using the boundary conditions,

$$\frac{d\sigma}{dt} = 0 \text{ at } \sigma = 0 \text{ and } \sigma = 1 \;. \tag{10.28}$$

The result is

$$\boxed{\frac{\partial p_s}{\partial t} = -\int_0^1\frac{1}{a\cos\phi}\left(\frac{\partial p_s u}{\partial \lambda} + \frac{\partial\left(p_s v\cos\phi\right)}{\partial \phi}\right)d\sigma = -\int_0^1\left(\frac{\partial p_s u}{\partial x} + \frac{\partial p_s v}{\partial y} - \frac{p_s v}{a}\tan\phi\right)d\sigma} \tag{10.29}$$

---

[9] Up to this point in the text the subscript σ indicates that the partial derivative is calculated with σ held constant. In the following we drop this subscript.

The set of equations (10.22), (10.23), (10.25), (10.26), (10.27) and (10.29) form a complete set of equations which, if the diabatic heating, J, is known and, if boundary conditions are specified, can be solved numerically on a grid of points distributed in a regular way in space and time (**figure 10.1**), by approximating the derivatives using **finite differences**. This yields a so-called "**primitive equation model**".

10.4 Formulation of a three-level primitive equation model

This section describes a **three level** version of a primitive equation model, which was developed by the author, assisted by several students [10], principally for educational purposes. A two level version of this model is described in Holton (1979) [11]. The atmosphere is **divided into three layers** separated by levels labeled 0, 2, 4 and 6 (see **figure 10.5**). These levels are defined in terms of σ. Level 0 corresponds to $\sigma = 0$; level 6 corresponds to $\sigma = 1$. Layers are referred to with the index k, while levels or surfaces are referred to with the index n.

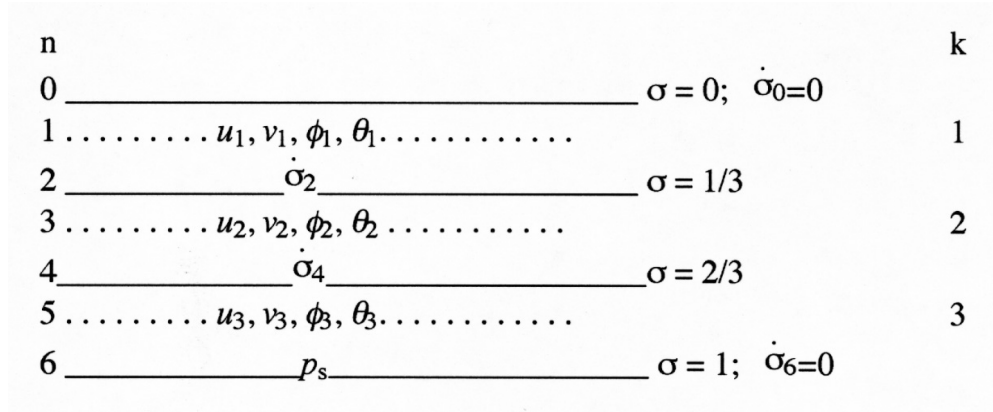| n		k
0 ——————————————— $\sigma = 0$; $\dot{\sigma}_0 = 0$		
1 . . . . $u_1, v_1, \phi_1, \theta_1$		1
2 ——————$\dot{\sigma}_2$——————— $\sigma = 1/3$		
3 . . . . $u_2, v_2, \phi_2, \theta_2$		2
4 ——————$\dot{\sigma}_4$——————— $\sigma = 2/3$		
5 . . . . $u_3, v_3, \phi_3, \theta_3$		3
6 ——————p_s——————— $\sigma = 1$; $\dot{\sigma}_6 = 0$		

FIGURE 10.5. Vertical structure of the three-level primitive equation model (see the text). Note that $n=2k-1$.

The momentum equation and the potential temperature equation are applied at levels $n=1$, 3 and 5, which in terms of σ are at the centre of the three layers. Thus, for example, eq. 10.25 takes the form

$$\left[\frac{\partial p_s \theta}{\partial t}\right]_k = \left[\frac{p_s v \theta}{a}\right]_k \tan\phi - \left[\frac{\partial p_s u \theta}{\partial x} + \frac{\partial p_s v \theta}{\partial y}\right]_k - \left[\frac{\partial}{\partial\sigma}\left(p_s \theta \frac{d\sigma}{dt}\right)\right]_k + \frac{p_s J_k}{\Pi_k} \; . \tag{10.30}$$

where k is the index of the layer. The vertical gradient of the vertical velocity is approximated with finite differences as follows.

$$\left[\frac{\partial}{\partial\sigma}\left(\frac{d\sigma}{dt}\right)\right]_n = \frac{\left(\frac{d\sigma}{dt}\right)_{n+1} - \left(\frac{d\sigma}{dt}\right)_{n-1}}{\Delta\sigma} \; , \tag{10.31}$$

---

[10] Koen Manders, Niels Zweers and Rosmarie de Wit.

[11] Holton, J.R. 1979. **An Introduction to Dynamic Meteorology. Second Edition**. Academic Press 391 pp. Strangely, the explicit description of this model was not included in later editions of this well-known textbook.

where $n=2k-1$ and $\Delta\sigma=1/3$. Writing the continuity equation (10.22) for layers 1, 2 and 3 with vertical derivatives replaced by centred difference, we obtain

$$\frac{\partial p_s}{\partial t} + \frac{1}{a\cos\phi}\left(\frac{\partial p_s u_1}{\partial\lambda} + \frac{\partial(p_s v_1\cos\phi)}{\partial\phi}\right) + \frac{p_s}{\Delta\sigma}\left[\frac{d\sigma}{dt}\right]_{n=2} = 0 \qquad (10.32)$$

$$\frac{\partial p_s}{\partial t} + \frac{1}{a\cos\phi}\left(\frac{\partial p_s u_2}{\partial\lambda} + \frac{\partial(p_s v_2\cos\phi)}{\partial\phi}\right) + \frac{p_s}{\Delta\sigma}\left(\left[\frac{d\sigma}{dt}\right]_{n=4} - \left[\frac{d\sigma}{dt}\right]_{n=2}\right) = 0 \qquad (10.33)$$

$$\frac{\partial p_s}{\partial t} + \frac{1}{a\cos\phi}\left(\frac{\partial p_s u_3}{\partial\lambda} + \frac{\partial(p_s v_3\cos\phi)}{\partial\phi}\right) - \frac{p_s}{\Delta\sigma}\left[\frac{d\sigma}{dt}\right]_{n=4} = 0 \qquad (10.34)$$

If equations (10.32), (10.33) and (10.34) are added we get the finite difference form of the surface pressure tendency equation:

$$\frac{\partial p_s}{\partial t} = -\frac{1}{a\cos\phi}\left(\frac{\partial\left(p_s(u_1+u_2+u_3)\right)}{\partial\lambda} + \frac{\partial\left(p_s(v_1+v_2+v_3)\cos\phi\right)}{\partial\phi}\right). \qquad (10.35)$$

Equations (10.32), (10.33) and (10.34) can also easily be manipulated to yield equations for the vertical velocity at levels 2 and 4. Subtracting (10.33) from (10.32) and subtracting (10.34) from (10.33) yields two equations. Multiplying the former equation by 2 and adding this to the latter equation yields:

$$\left[\frac{d\sigma}{dt}\right]_2 = \frac{-\Delta\sigma}{3p_s a\cos\phi}\left(2\frac{\partial p_s u_1}{\partial\lambda} - \frac{\partial p_s u_2}{\partial\lambda} - \frac{\partial p_s u_3}{\partial\lambda} + 2\frac{\partial p_s v_1\cos\phi}{\partial\phi} - \frac{\partial p_s v_2\cos\phi}{\partial\phi} - \frac{\partial p_s v_3\cos\phi}{\partial\phi}\right) \qquad (10.36)$$

Multiplying the latter equation by 2 and adding this to the former equation yields:

$$\left[\frac{d\sigma}{dt}\right]_4 = \frac{-\Delta\sigma}{3p_s a\cos\phi}\left(\frac{\partial p_s u_1}{\partial\lambda} + \frac{\partial p_s u_2}{\partial\lambda} - 2\frac{\partial p_s u_3}{\partial\lambda} + \frac{\partial p_s v_1\cos\phi}{\partial\phi} + \frac{\partial p_s v_2\cos\phi}{\partial\phi} - 2\frac{\partial p_s v_3\cos\phi}{\partial\phi}\right) \qquad (10.37)$$

The geopotential in the different layers must be determined from the potential temperature using the hydrostatic relation (10.23). Here we use an alternative form, i.e.

$$\frac{\partial\Phi}{\partial p^\kappa} = \frac{\partial\Phi}{\partial p}\frac{\partial p}{\partial p^\kappa} = \frac{-\alpha}{\kappa p^{\kappa-1}} = \frac{-RT}{\kappa p^\kappa} = \frac{-R\theta}{\kappa p^\kappa}\left(\frac{p}{p_{ref}}\right)^\kappa = \frac{-c_p\theta}{p_{ref}^\kappa}, \qquad (10.38)$$

where we have used the hydrostatic relation in pressure coordinates, the equation of state and the definition of potential temperature. This form of the hydrostatic relation is easier to approximate with finite differences than (10.23). Applying (10.38) at levels 2 and 4 yields (subscripts indicate the level, n)

$$\Phi_1 - \Phi_3 = \frac{-c_p \theta_2}{p_{ref}^\kappa}\left(p_1^\kappa - p_3^\kappa\right) \equiv A; \; \Phi_3 - \Phi_5 = \frac{-c_p \theta_4}{p_{ref}^\kappa}\left(p_3^\kappa - p_5^\kappa\right) \equiv B. \tag{10.39}$$

We now ascertain that (using the equation of state and eq. 10.23)

$$\frac{\partial \sigma \Phi}{\partial \sigma} = \sigma \frac{\partial \Phi}{\partial \sigma} + \Phi = \Phi - p\alpha. \tag{10.40}$$

Applying this equation to layers 1, 2 and 3 (i.e. levels n=1, 3 and 5), and adding the resulting three equations yields (subscripts indicate the level, n)

$$\Phi_1 + \Phi_3 + \Phi_5 = 3\Phi_6 + p_s\left(\sigma_1\alpha_1 + \sigma_3\alpha_3 + \sigma_5\alpha_5\right) \equiv C. \tag{10.41}$$

The geopotential at the Earth's surface, Φ_6, is a known function of x and y. Combining equations (10.39) and (10.41), we get the following expressions for the geopotential at levels 1, 3 and 5:

$$\Phi_1 = \frac{1}{3}(2A + B + C); \; \Phi_3 = \frac{1}{3}(-A + B + C); \; \Phi_5 = \frac{1}{3}(-A - 2B + C). \tag{10.42}$$

10.5 The multilevel primitive equation model

It is straightforward to construct a version of the model with any number of layers. The only complication comes with the solution of the hydrostatic equation. This section decribes the method of solution of the hydrostatic equation if the number of layers is equal to K. The discrete form of eq. 10.38 is

$$\frac{\Phi_{k+1} - \Phi_k}{p_{k+1}^\kappa - p_k^\kappa} = -\frac{c_p\left(\theta_{k+1} + \theta_k\right)}{2p_{ref}^\kappa}. \tag{10.43}$$

The discrete form of eq. 10.40 now becomes

$$\frac{\Phi_s}{\Delta \sigma} = \sum_{k=1}^{K}\left(\Phi_k - p_s\sigma_k\alpha_k\right), \tag{10.44}$$

where Φ_s is the geopotential at the surface of the Earth. The above two equations form a set of N equations with N unknowns, which can be written compactly as

$$\begin{pmatrix} \Phi_1 \\ . \\ . \\ . \\ . \\ \Phi_K \end{pmatrix} = M^{-1}\begin{pmatrix} X_1 \\ . \\ . \\ . \\ . \\ X_K \end{pmatrix}, \tag{10.45}$$

where

$$X_k = -\frac{1}{2}\left(\Pi_{k+1} - \Pi_k\right)\left(\theta_{k+1} + \theta_k\right)$$

for $k=1\ldots K$-1, (the Exner function, $\Pi=c_pT/\theta$, see section 1.13) and

$$X_K = \frac{\Phi_s}{\Delta\sigma} + p_s \sum_{k=1}^{K}\left(\sigma_k\alpha_k\right) \tag{10.46}$$

and the matrix M is defined as

$$M = \begin{pmatrix} -1 & 1 & 0 & . & . & . & 0 \\ 0 & -1 & 1 & 0 & & & 0 \\ . & & & & & & . \\ . & & & & & & . \\ . & & & & & & . \\ 0 & . & . & . & 0 & -1 & 1 \\ 1 & 1 & . & . & . & 1 & 1 \end{pmatrix}. \tag{10.47}$$

The geopotential at each level is found from eq. 10.45 after inverting M.

The local tendency of surface pressure is calculated from (10.29) with knowledge of the wind, after which the σ–vertical velocity is calculated by applying (10.22) to successive levels from top to bottom (or vice versa) (see e.g. eqs. 10.36 and 10.37).

10.6 Domain, numerical approximations and initial condition

To simulate the life cycle of an unstable baroclinic wave in mid-latitudes (section 10.7) we assume that the **horizontal domain is a "channel", with a length, L, in the longitudinal direction, with periodic boundary conditions on the west and east side**. At the **southern and the northern boundaries the first and second order derivatives of all quantities perpendicular to the boundary are set to zero**. The **grid** is a so-called "**lat-lon**" grid with dimi=72 points in the zonal direction and dimj=116 points in the meridional direction. The gridpoint distance, Δx in the zonal direction depends on L, according to $\Delta x=L/$dimi. In this section we neglect the convergence of the meridians, which implies that $\Delta x=$constant. In the single simulation, discussed in section 10.7, $\Delta x\approx65.5$ km, which is equivalent to $L=60°$[longitude] at $45°$ latitude with dimi=72. The grid distance in the latitudinal direction is $\Delta y=0.6°\approx66.6$ km. The **curvature of the Earth's surface is neglected**. The Coriolis parameter, $f=f_0=10^{-4}$ s^{-1}. With the periodic boundary conditions in east-west direction, the model is able to simulate the growth and decay (i.e. the life cycle) of an unstable baroclinic disturbance with a prescribed wavelength, L, at reduced computational cost. The wave moves out of the domain at the east side and re-enters at the western side, or vice-versa.

The advection-, pressure gradient- and Coriolis terms in the momentum- and potential temperature equation (10.25-27) are approximated with the **MacCormack scheme**[12], which

---

[12] Mendez-Nunez, L.R., and J.J. Caroll, 1993: Comparison of leapfrog, Smolarkiewicz, and MacCormack schemes applied to nonlinear equations. **Mon.Wea.Rev**., 121, 565-578.

is good at handling large gradients. The time step is kept very small (4 s [13]). This is because horizontally propagating acoustic (Lamb) waves (chapter 3) are part of the solution, while **diffusion and surface friction**, which are usually incorporated to damp high frequency and small scale variations, are neglected. The surface pressure equation is solved using centred differences in space and the same two-step in time ("predictor-corrector") scheme in time, as in the MacCormack scheme.

The fields of p_s, p_su, p_sv, and $p_s\theta$ are smoothed with a horizontal five-point smoother[14] once every 3 hours of simulation time. This filters out so-called "2Δx" waves, which, despite the small time step tend to appear after three hours of simulation.

10.7 The life-cycle of an unstable adiabatic baroclinic planetary wave: fronts and vertical motion

It is instructive to start this section by quoting one of the chief discoverers of baroclinic instability (Charney, 1947)[15]. In a conversation with George Platzman in 1980 (Lindzen et al., 1990)[16], Platzman posed him the following question:

Platzman: Do you think this problem (baroclinic instability) has been solved?

Charney: Oh, I think that if you talk about the stability of zonal flow, purely and simply, of the simple zonal flow, I think it has been largely solved by now. But if you take the finite amplitude problem, or the relationship of the upper wave and the frontal wave, if you carry them to the realm where they can be observed so you must necessarily deal with the finite-amplitude problem, I think that they're far from having been solved. And it has always been a matter of puzzlement to me why the linear solutions do bear a resemblance to the observed motions. Especially if you used some of the modern filtering techniques, let's say time filtering, so that you can manage to look at only the motions with a certain frequency range.

In 1980 the solution of the problem of a growing baroclinic wave and its relation to the observed life-cycle of middle latitude cyclones was still in its infancy. Of course, there were conceptual models largely due to the Bergen School, based on the pioneering work by J. Bjerknes[17], published in 1919, but the theory explaining the coarse of events (the life-cycle) as depicted in **figure 10.3** was just beginning to be developed [18]. Starting in the 1970's numerical simulations of the growth of a baroclinic wave were performed, which, together with the emerging adulthood of the theory of frontogenesis, gave considerable insight into the dynamics of middle latitude cyclones.

---

[13] A time step of 4 seconds seems unnecessarily small! A similar operational hydrostatic model with a grid distance of about 60 km employs a time step in order of minutes, but these models require many filters (in space and time) that damp numerical oscillations and instabilities.

[14] Haltiner, G.J., and R.T. Williams, 1980: **Numerical Prediction and Dynamic Meteorology.** Second edition. John Wiley & Sons. 477 pp, p. 397.

[15] Charney, J.G., 1947: The dynamics of long waves in a westerly current. **J.Meteorol**., 4, 135-163.

[16] Lindzen, S., E.N. Lorenz and G.W. Platzman, (eds), 1990: **The Atmosphere – A Challenge. The Science of Jules Gregory Charney** (American Meteorological Society).

[17] Bjerknes, J., 1919: On the structure of moving cyclones. **Geofys.Publ.**, **1**, 8 pp.

[18] Davies, H.C., 1997: Emergence of the mainstream cyclogenesis theories. **Meteorol.Zeitschrift**, N.F. **6**, 261-274. This article gives an interesting account of the history of cyclogenesis theories.

   This section discusses the results of one single numerical simulation of the life cycle of an unstable baroclinic wave in a periodic channel on an "*f*"-plane (*f* is constant), using a 36-level version of the primitive equation model.

   The model is initialised with a prescribed three-dimensional distribution of geopotential, similar to the geopotential distribution given by eq. 9.78a. However, the background state of a uniform zonal flow, in a geostrophic equilibrium, that is prescribed in the linear analysis (section 9.7), and also in connection with solution of the omega-eqaution in section 9.9 (eq. 9.78a), is definitely not realistic. In reality a zone of intense meridional temperature contrast is usually concentrated in a relatively narrow band running from west to east and meandering in the meridional direction. The important question of how this intense temperature contrast is formed is not treated here, but in chapter 12.

   Here, the following more realistic initial geopotential distribution is prescribed:

$$\Phi(x,y,p,t) = \Phi_0(p) - y_{scale} f_0 U_0 \tanh\left(\frac{y - y_0}{y_{scale}}\right)\cos\left(\frac{\pi p}{2 p_0}\right). \tag{10.48}$$

In other words, the linear dependence of Φ on y (eq. 9.78a) has been replaced by a hyperbolic tangent y-dependence around the central latitude, $y=y_0$. This restricts the temperature gradient to the range $y_0-y_{scale}<y<y_0+y_{scale}$. Therefore, y_{scale} represents the horizontal width of the front and associated jet. The pressure at the Earth's surface at $t=0$ is constant, i.e. at the Earth's surface, $p=p_s(x,y,t)=p_0=1000$ hPa. This implies that, initially, surfaces of equal sigma are also surfaces of equal pressure. It also implies that the geostrophic wind is zero at the Earth's surface.

   The geopotential at $y=y_0$, $\Phi_0(p)$, is determined from the integration of the hydrostatic equation after prescribing the temperature at $y=y_0$ according to the formula,

$$T_0(z) = T_0(0) - \Gamma_0 z \ , \tag{10.50}$$

where $T_0(0)$ is the temperature at $t=0$, at $z=0$ (the Earth's surface) and Γ_0 is the **temperature lapse rate**, i.e., using the equation of state, $p=\rho RT$, and hydrostatic balance, $\partial p/\partial z=-\rho g$,

$$\Gamma_0 = -\frac{dT_0}{dz} = \rho_0 g \frac{dT_0}{dp} = \frac{pg}{RT_0}\frac{dT_0}{dp} = \frac{g}{R}\frac{d\ln T_0}{d\ln p},$$

or

$$d\ln T_0 = \frac{R\Gamma_0}{g} d\ln p \ .^{19} \tag{10.51}$$

Γ_0 is assumed to be constant (=6.5 K km^{-1}).

   The geostrophic wind, associated with (10.48), is

---

[19] If we impose a constant lapse rate of 6.5 K km^{-1}, which is typical for the troposphere, and a surface temperature of 285 K, the temperature will go below absolute zero above about $z=44$ km! The highest model level is located at $\sigma=14$ hPa, which corresponds to $z\approx27$ km. A constant lapse rate of 6.5 K km^{-1} will, thus, not lead to physically unrealistic model temperatures as long as the surface temperature is higher than 175 K.
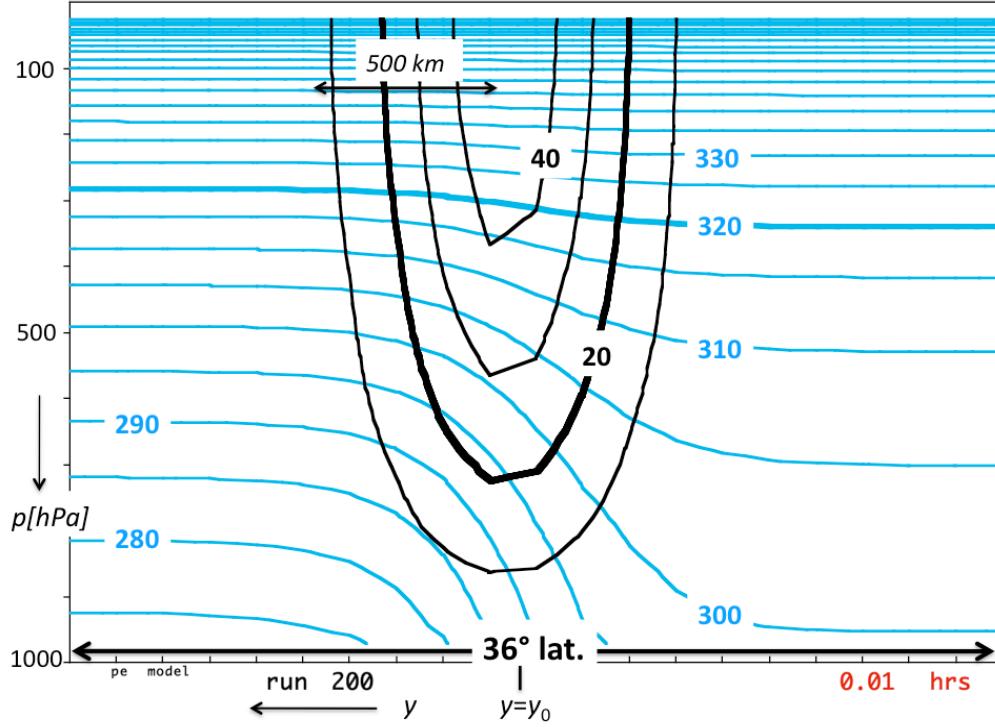
FIGURE 10.6. Geostrophic zonal wind (according to eq. 10.52, with U_0=50 m s^{-1} and y_{scale}=500 km, and potential temperature, according to thermal wind balance, as a function of latitude and pressure at initial time. Labels are indicated in m/s and K, respectively. The 295 K isentrope intersects the surface of the earth, while the 300 K isentrope does not. Therefore, all isentropes below the 295 K isentrope belong to the "Underworld", while all isentropes above the 300 K isentrope belong to the "Middleworld" or "Overworld" (**figure 1.48**).

$$u_g = -\frac{1}{f_0}\frac{\partial \Phi}{\partial y} = U_0 \cos\left(\frac{\pi p}{2 p_0}\right)\left\{1 - \tanh^2\left(\frac{y - y_0}{y_{scale}}\right)\right\} . \qquad (10.52)$$

In terms of latitude, ϕ, this can be expressed as,

$$u_g = U_0 \cos\left(\frac{\pi p}{2 p_0}\right)\left\{1 - \tanh^2\left(\frac{\phi - \phi_0}{\phi_{scale}}\right)\right\} . \qquad (10.53)$$

According to (10.53), the zonal geostrophic wind peaks at latitude, $\phi=\phi_0$, and falls off to zero if $|\phi\text{-}\phi_0|>\phi_{scale}$. The geostrophic wind, according to eq. 10.52, assuming that U_0=50 m s^{-1} and y_{scale}=500 km, as a function of latitude and pressure, is shown in **figure 10.6**. Also shown is the potential temperature, which is calculated from (10.53) by integrating the equation for thermal wind balance (eq. 9.81):

$$\frac{\partial T}{\partial y} = \frac{p f_0}{R}\frac{\partial u_g}{\partial p} ,$$

assuming a temperature profile at $y=y_0$, given by eq. 10.50 with a constant lapse rate, Γ_0=6.5 K km^{-1} and with T_0=285 K.
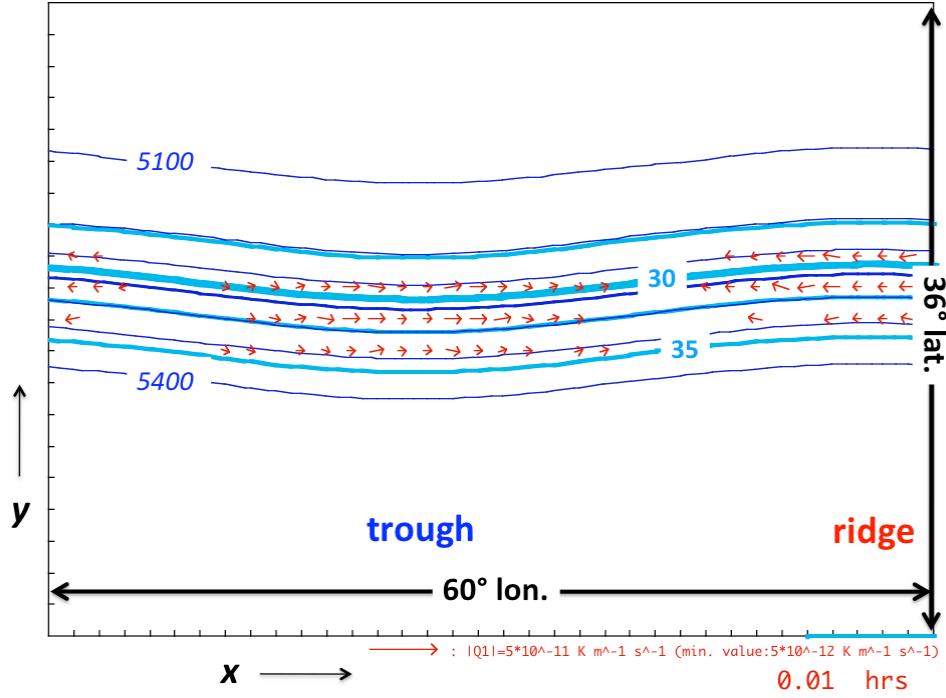
FIGURE 10.7. Geopotential height (thin solid **dark blue** lines; contour interval is 50 m, thick line corresponds to 5250 m) and *potential* temperature (**cyan** lines; contour interval is 2.5 K, thick line corresponds to 30°C) at 513 hPa at t=0. The vertical axis corresponds to latitude (distance from bottom to top is 36°). The horizontal axis corresponds to longitude (distance from left to right is L_x=60°). Boundary conditions at the western and eastern boundary are periodic. The southern and northern boundaries are "open". The computational domain in the meridional direction spans a distance of 69°. Therefore, the southern at northern boundaries are not shown in this figure. Geostrophic Q-vectors (**red arrows**) are shown only if the absolute value exceeds 5×10^{-12} K m^{-1} s^{-1}. Other parameter values are, C=1° lat (eq. 10.59), L_x=60°, ϕ_{00}=45°, ϕ_{scale}=4.5°=500 km, U=50 m s^{-1}, f_0=10^{-4} s^{-1}, Γ_0=0.0065 K m^{-1} and $T_0(z$=0)=285 K (eq. 10.50).

If we neglect the curvature of the coordinate system and assume that the Coriolis parameter, f_0, is constant, the model equations, are as follows:

$$\frac{\partial p_s}{\partial t} + \frac{1}{a\cos\phi}\left(\frac{\partial p_s u}{\partial \lambda} + \frac{\partial(p_s v \cos\phi)}{\partial \phi}\right) + p_s \frac{\partial}{\partial \sigma}\left(\frac{d\sigma}{dt}\right) = 0 \; ;$$
(10.54)

$$\frac{\partial p_s \theta}{\partial t} = -\left(\frac{\partial p_s u\theta}{\partial x} + \frac{\partial p_s v\theta}{\partial y}\right) - \frac{\partial}{\partial \sigma}\left(p_s\theta\frac{d\sigma}{dt}\right) \; ;$$
(10.55)

$$\frac{\partial p_s u}{\partial t} = -\left(\frac{\partial p_s u^2}{\partial x} + \frac{\partial p_s uv}{\partial y}\right) - \frac{\partial}{\partial \sigma}\left(p_s u\frac{d\sigma}{dt}\right) + f_0 p_s v - \frac{1}{a\cos\phi}\left(p_s \frac{\partial \Phi}{\partial \lambda} + RT\frac{\partial p_s}{\partial \lambda}\right) \; ;$$
(10.56)

$$\frac{\partial p_s v}{\partial t} = -\left(\frac{\partial p_s uv}{\partial x} + \frac{\partial p_s v^2}{\partial y}\right) - \frac{\partial}{\partial \sigma}\left(p_s u\frac{d\sigma}{dt}\right) - f_0 p_s u - \frac{1}{a}\left(p_s \frac{\partial \Phi}{\partial \phi} + RT\frac{\partial p_s}{\partial \phi}\right) \; ;$$
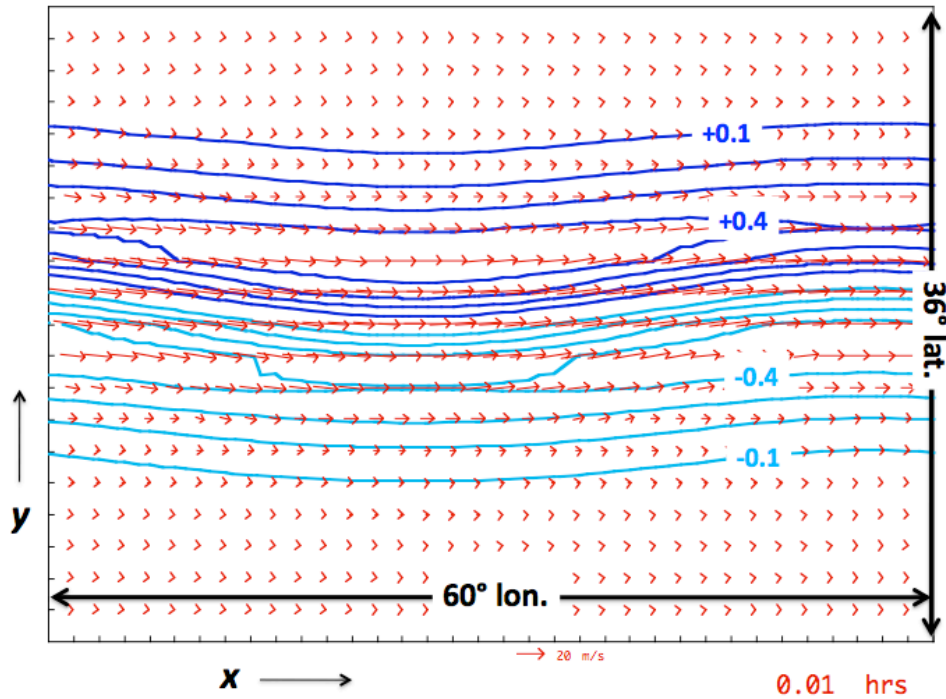(10.57)

FIGURE 10.8. The wind vectors and relative vorticity (contour interval is 0.1×10^{-4} s^{-1}, zero-contour not shown, solid/**blue**: **positive** and grey/**cyan**: **negative**, at 513 hPa at $t=0$. Labels are in units of 10^{-4} s^{-1}. See **figure 10.7** for the parameter-values.

$$\frac{\partial p_s}{\partial t} = -\int_0^1 \frac{1}{a\cos\phi}\left(\frac{\partial p_s u}{\partial \lambda} + \frac{\partial(p_s v \cos\phi)}{\partial \phi}\right) d\sigma = -\int_0^1 \left(\frac{\partial p_s u}{\partial x} + \frac{\partial p_s v}{\partial y}\right) d\sigma \quad . \tag{10.58}$$

The zonal flow is perturbed, by making the reference-latitude, ϕ_0, in eq. 10.53 a function of longitude, as follows.

$$\phi_0(x) = \phi_{00} + C\sin(2\pi x / L_x), \tag{10.59}$$

where ϕ_{00} is the central latitude, C is the latitudinal amplitude (in degrees) of the meander in the jet stream and L_x the horizontal extent of the domain, or the wavelength of the initial meander, or wave, in the jet stream. The central latitude is consistent with the chosen value of the Coriois parameter, in the case here: $f=f_0=10^{-4}$ s^{-1}, which implies that $\phi_{00}\approx 45°$.

The initial geostrophic velocity distribution for $p=513$ hPa is shown in **figure 10.8**. If the prescribed temperature is a function of only latitude and height, the associated geostrophic flow is straight perfectly eastward. This is an exact balanced state. However, if the geopotential distribution is perturbed slightly, by making the reference-latitude, ϕ_0, a function of longitude (eq. 10.59), the associated geostrophic flow does not represent an exact balanced state, because of the curvature of the flow. The imbalance is manifest in the Q_g-vectors (**figure 10.7**), which point in eastward direction near the trough axis, and in westward direction near the ridge axis (section 9.8) and thus converge (diverge) to the east (west) of the trough. We know from the omega-equation (9.31) that this will lead to vertical motion.

If the atmosphere is in thermal wind balance, the baroclinic zone, which is centred

around $y=y_0$, is associated with a relatively narrow jet. On the northern side of this jet relative vorticity is positive (in the northern hemisphere), while on its southern side relative vorticity is negative (**figure 10.8**).

In **figure 10.9**, the initial condition is shown in a longitudinal cross-section along the central latitude, $\phi=\phi_{00}$ or $y=y_0$ (**figure 10.6**). Note that this initial state is **not the most unstable according to linear theory**, since the wave is not "tilted" in the vertical (section 9.7). Nevertheless, the trough is associated with $\partial v_g/\partial x>0$, while the ridge is associate with with $\partial v_g/\partial x<0$. The Q-vector forcing, observed in **figure 10.7**, is due to the term,

$$Q_{g1} = -\frac{\partial v_g}{\partial x}\frac{\partial T}{\partial y} \ . \tag{10.60}$$

which yields Q-vectors pointing in opposite directions in, respectively the trough (eastward) and the ridge (westward), as was explained in sections 9.8 and 9.9. This represents a slight imbalance, which is the seminal state of a growing baroclinic wave. Remember that we have set $\beta=0$, so that, according to the linear analysis of small perturbations superposed on a horizontally homogeneous thermal wind, all waves with a longitudinal wavelength longer than a critical wavelength are baroclinically unstable (eq. 9.62). Indeed, the **adiabatic**, inviscid (no heating, no friction) evolution, simulated by the model, shows the development of a very realistic cyclone within 3 to 4 days (**figure 10.14**).

The **phase difference** between the thermal wave and the geopotential wave, as well as the **vertical phase tilt of the trough**, observed in **figure 10.10**, are not due to a fortuitous conjunction of circumstances, but are actually **created by the wave itself** (**figure 10.8**).
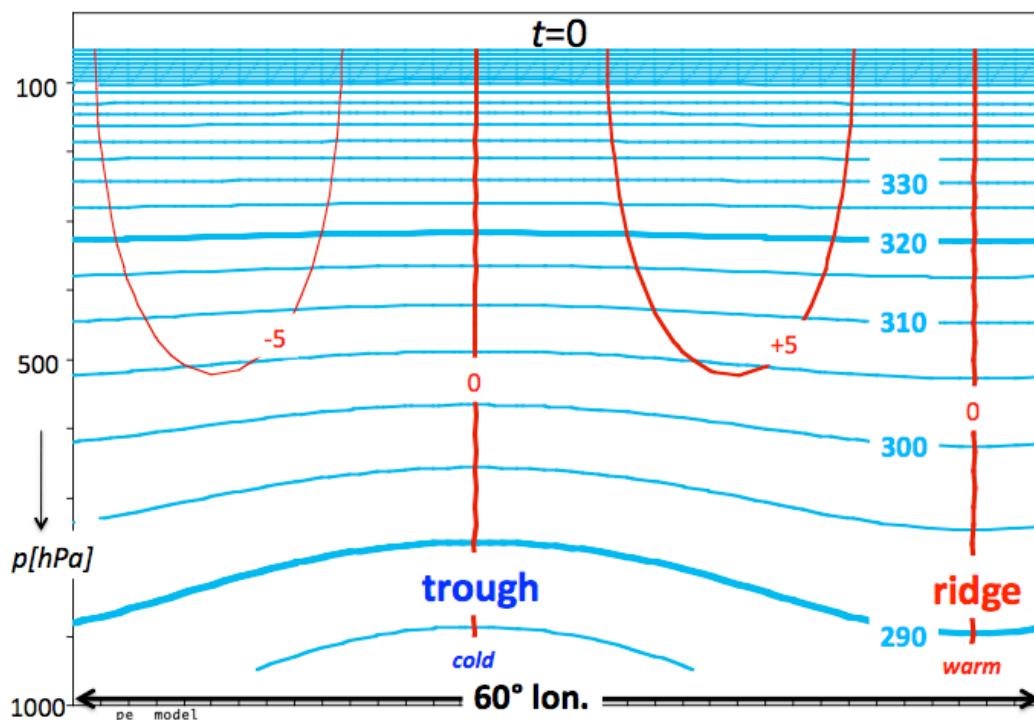

FIGURE 10.9. The meridional component of the geostrophic wind (**red contours, labeled in m s^{-1}, positive is northward**) and the potential temperature (**cyan contours, labeled in K**) as a function of longitude and pressure at the central latitude, $\phi=\phi_{00}$.
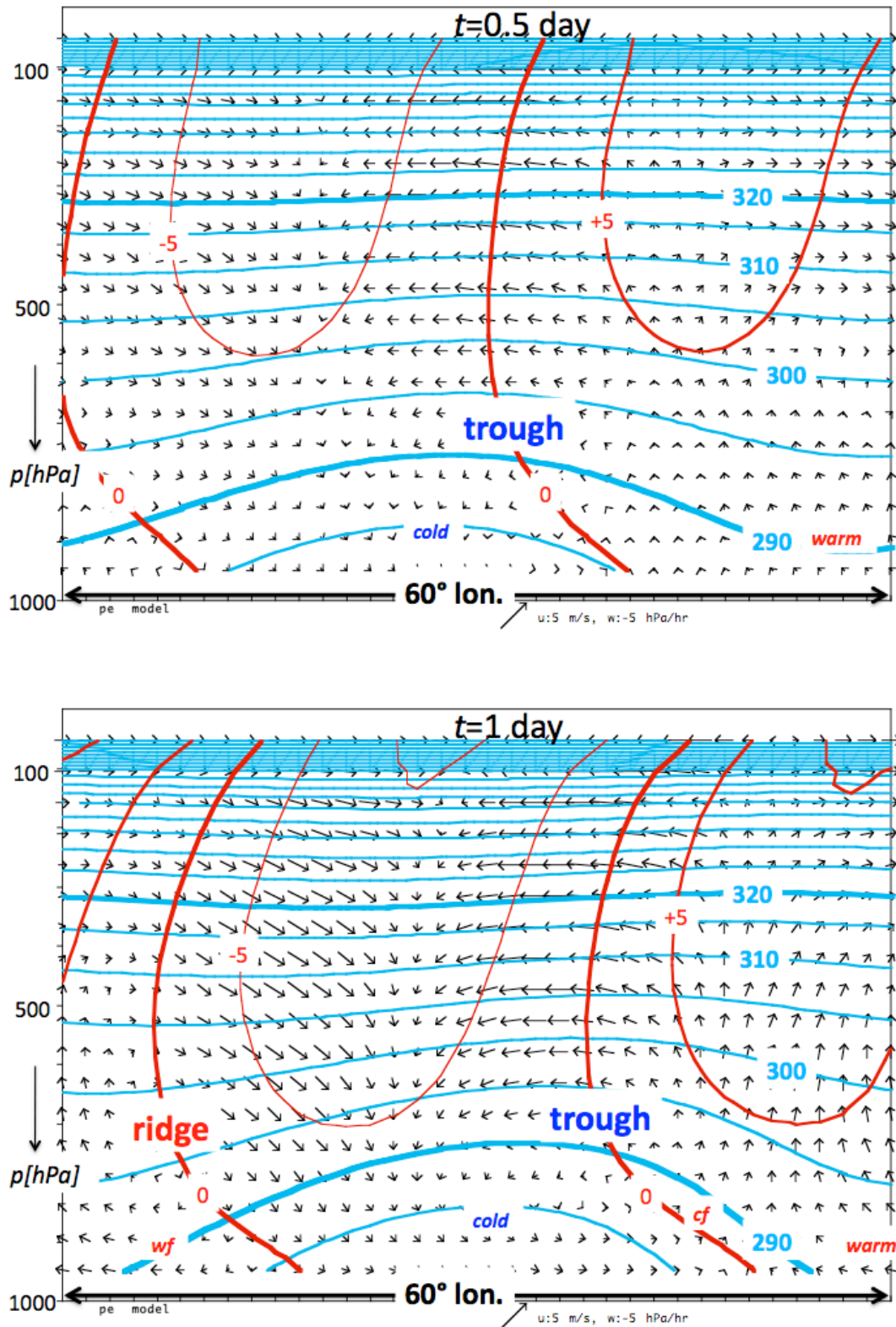
FIGURE 10.10. Meridional component of the geostrophic wind (**red contours, labeled in m s⁻¹, positive is northward**), the potential temperature (**cyan contours, labeled in K**) and wind-vector in the plane of the cross-section, relative to the zonal average wind-vector, as a function of longitude and pressure at the central latitude, $\phi=\phi_{00}$, after half a day (upper panel) and after 1 day (lower panel). The warm front and the cold front are indicated by "*wf*" and by "*cf*" respectively.
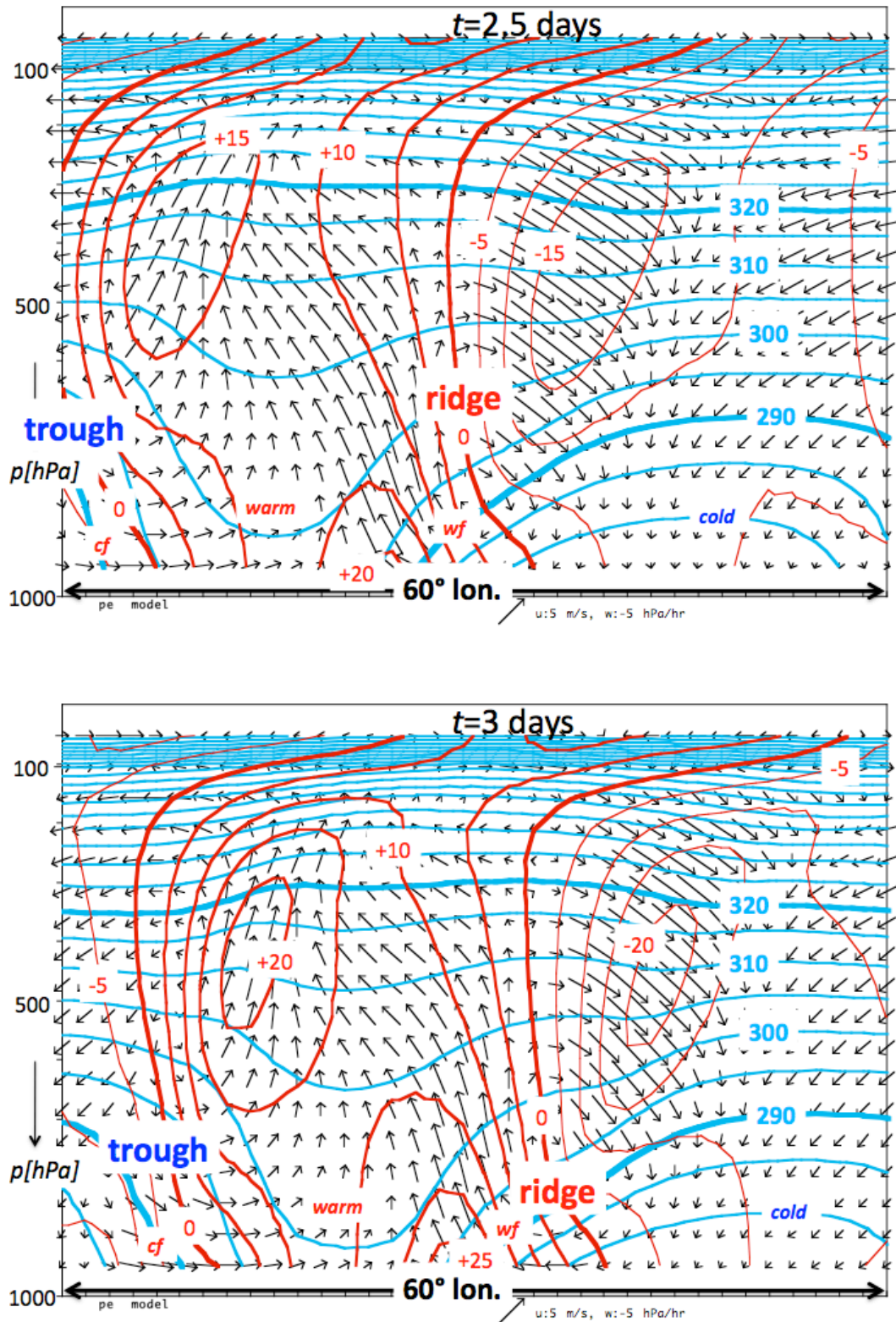
FIGURE 10.11. Same as **figure 10.9**, except for after *t*=1.5 days (upper panel) and *t*=2 days (lower panel). Note that the warm sector is getting warmer, while the cold sector is getting colder. The implies that the zonal temperature gradients, $|\partial T/\partial x|$, between the cold sector and the warm sector, is increasing in time. Remember: **air parcels do not cross isentropes!**

FIGURE 10.12. As **figure 10.10** and **10.11**, except for *t*=2.5 days (upper panel) and *t*=3 days (lower panel). A low-level jet with northward winds has developed at the warm front. Likewise, an upper-level jet with northward winds has developed above the cold front. Air parcels do not cross isentropes! Nearly all air, which is confined below the 290 K isentrope, i.e. air in the "Underworld", flows equatorward, as part of a "**cold air outbreak**", while air in the "Middleworld" or Overworld" flows *both* equatorward and poleward.

The growth of the wave-amplitude during the first three days is shown in longitudinal cross-sections along the central latitude in **figures 10.10-10-12**. The initial development of vertical motion in the longitudinal plane (**figure 10.10**) is qualitatively in agreement with the solution of the omega-equation (9.31) (**figure 9.16**), i.e. we observe upward motion to the east of the trough and downward motion to the west of the trough. Upward motion leads to vortex stretching at low levels, which contributes to a positive tendency of relative vorticity. Since this effect is weaker at higher levels, the trough axis tends to develop a westward tilt with increasing height at low levels. At higher levels, the tilt of the trough-axis is in the opposite direction, i.e. eastward with increasing height. This is due to the effect of increasing (with height) eastward advection of relative vorticity by the strong eastward wind in the jet.

We also observe (**figures 10.9-10-11**) that, at $y=y_0$, the cold sector becomes colder and that warm sector becomes warmer, implying frontogenesis *in the y-direction*. In the middle stage of the life-cycle of the unstable baroclinic wave (after 2 days) two northward jets appear, one at upper levels above the cold front and the other at low levels at the warm front.

In the horizontal cross-sections (**figures 10.13** and **10.14**) at 865 hPa (about 1200 m above the Earth's surface) we observe the development of a cyclone and an anticyclone. We also see a very realistic temperature distribution, with a warm front, a cold front and a back-bent front in accordance with the portrayal in **figure 10.3**.

During the first two days of the evolution the Q_g-vectors point in a direction that is approximately parallel to the isentropes (**figure 10.7**), indicating that the frontogenetic process is associated principally with the turning of the isentropes, and much less with the material change with time of the absolute value of the temperature gradient (section 1.37).

On days 3 and 4 **the amplitude of the Q_g-vectors has in general increased**. Q_g-vectors point up the temperature gradient almost everywhere along the fronts. This indicates a positive tendency of the absolute temperature gradient. The only exception is the back-bent front, where the Q_g-vectors are approximately parallel to the isotherms, which indicates that frontogenesis here is related to the rotation of the isentropes (changing direction of the temperature gradient), which is not surprising, since the back-bent front is located in the core of the cyclone.

On days 3 and 4 we also observe (**figure 10.14**) strongly diverging Q_g-vectors in the region between the cold front and the back-bent front. In accordance with the solution of the omega eq. (9.31), which states that downward motion should occur in a region of Q_g-vector divergence, motion is indeed downward in this region (**figure 10.15**). This explains the existence of the "dry intrusion" (**figure 9.6d**) in which dry stratospheric air descends and sometimes reaches relatively low levels in the troposphere. Also in accordance with the solution of the omega eq. 9.31, we observe upward (downward) motion on the warm (cold) side of the cold front.

Due to the westward tilt of both the trough- and ridge axis, nearly all air in the Underworld, confined below the 290 K isentrope, flows equatorward. This equatorward flow is referred to as a "**cold air outbreak**", in which the low level potentially cold air mass on the poleward side of the front is "discharged", leading to a reduction of the zonal mean surface pressure on the poleward side of the front and an increase of the associated surface zonal component of the geostrophic wind (**figure 10.19**).

A schematic picture of the general nature of the motion in a mature cyclone and its surroundings is shown in **figure 10.16**, looking northwards in the northern hemisphere. The descending air west of the surface low, on reaching middle levels, splits into two branches, A and B, turning anticyclonically and cyclonically, respectively. Branch B represents the dry intrusion. Air originating at lower levels in the warm sector, equatorward of the surface low, rises and splits into two branches C and D.
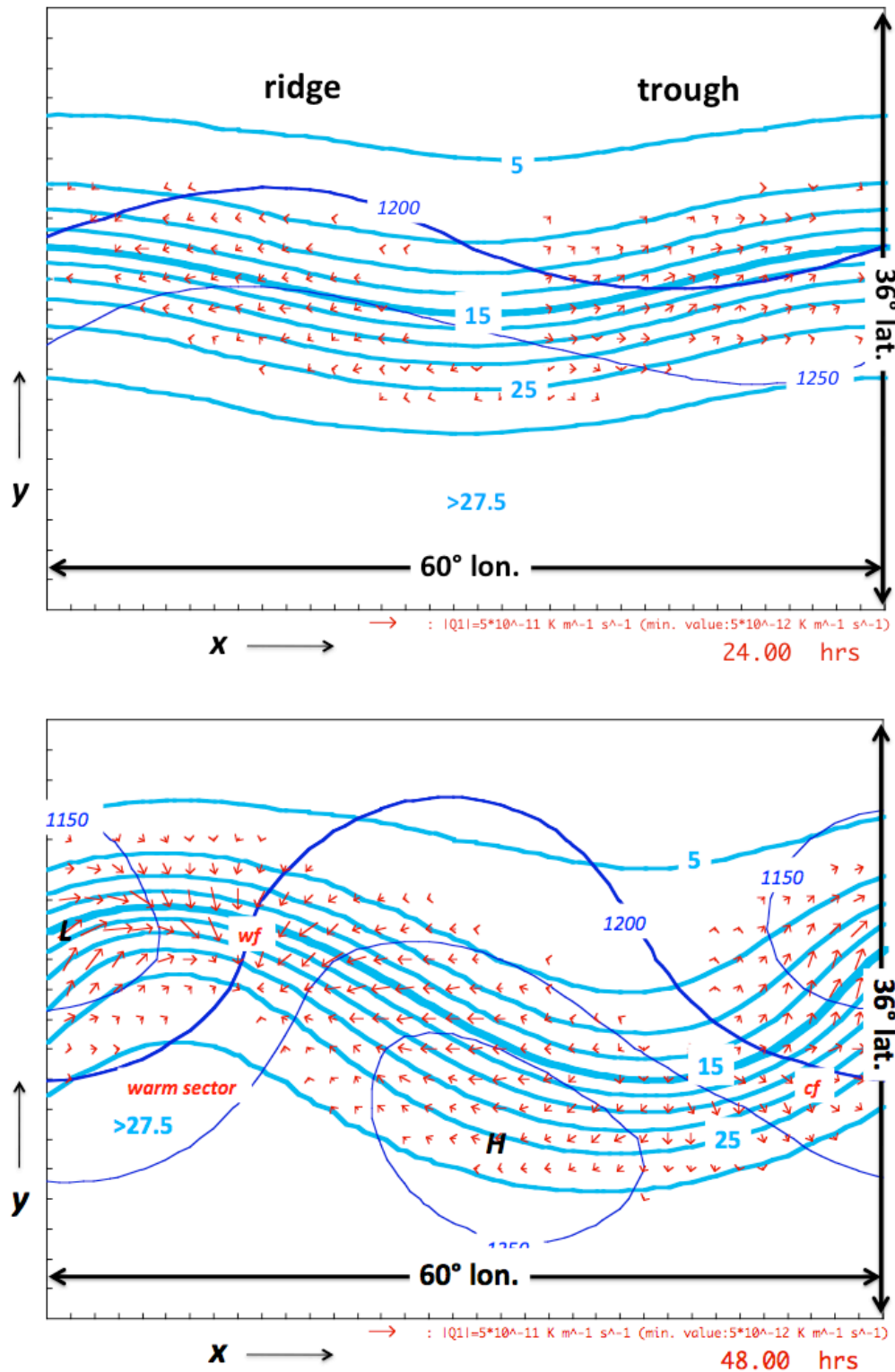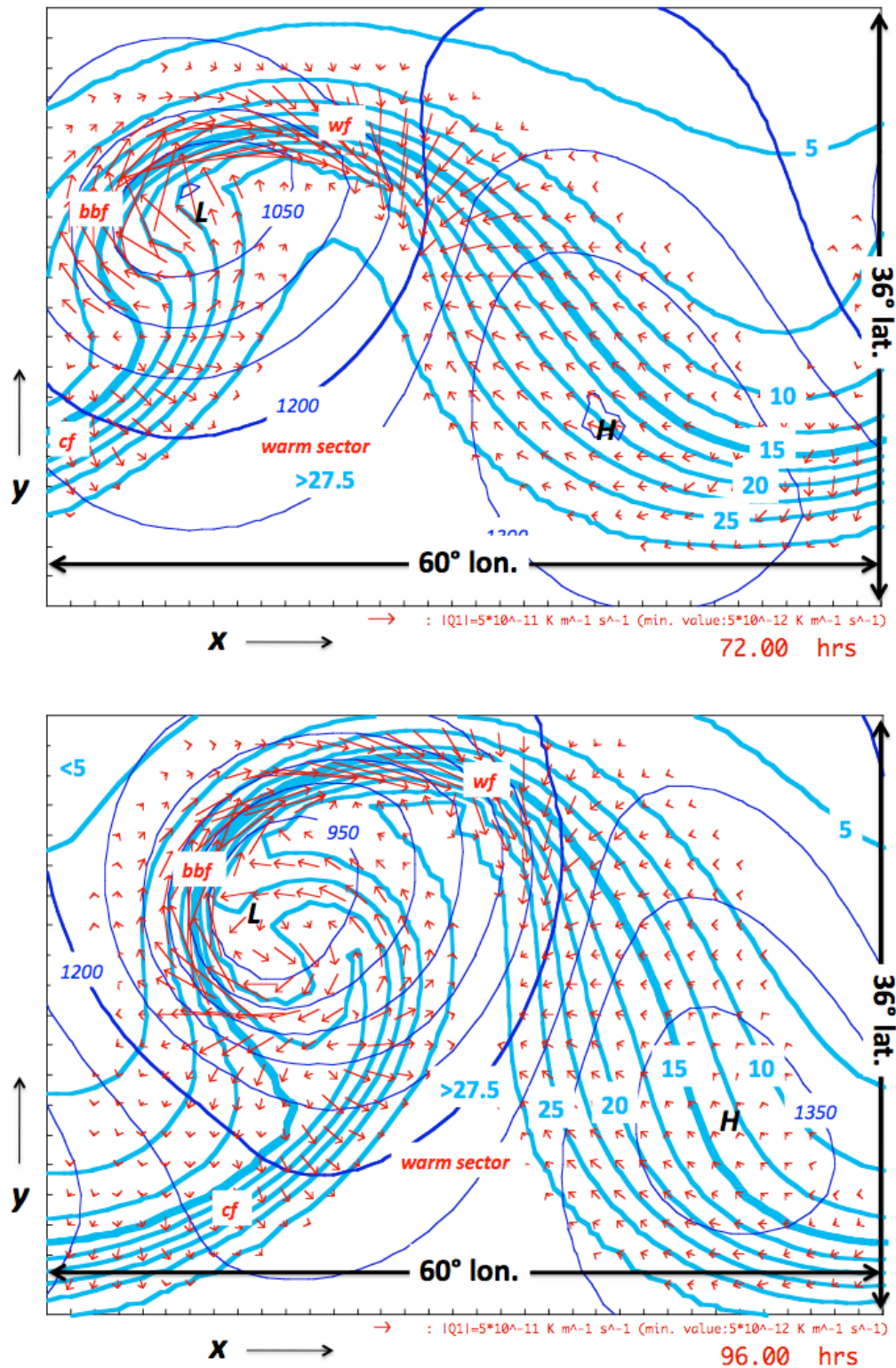
FIGURE 10.13. Early stage of the life-cycle of an adiabatic inviscid baroclinic wave at 865 hPa as simulated by a 36-level primitive equation model. The geopotential height, indicated by thin solid **dark blue** lines (contour interval is 50 m, thick line corresponds to 5200 m) and the potential temperature indicated by **cyan lines** (contour interval is 2.5 K, thick line corresponds to 15 °C). Geostrophic Q-vectors (**red arrows**) are shown only if the absolute value exceeds 5×10^{-12} K m^{-1} s^{-1}. The vertical axis corresponds to latitude. The horizontal axis corresponds to longitude. The boundary conditions at the western and eastern boundary are periodic. More information is given in the caption of **figure 10.7**.

26

FIGURE 10.14. Mature stage of the life-cycle of an adiabatic inviscid baroclinic wave at 865 hPa as simulated by a 36-level primitive equation model. More information is given in the caption of **figure 10.13**. Note the change in scale of the Q_g-vectors (red arrows) in this figure compared to **figure 10.13**. The warm front is indicated by "*wf*". The cold front is indicated by "*cf*". The back-bent front is indicated by "*bbf*". On the following web site you will find animations of this integration ("run 200"): http://www.staff.science.uu.nl/~delde102/BaroclinicLifeCycle.htm.
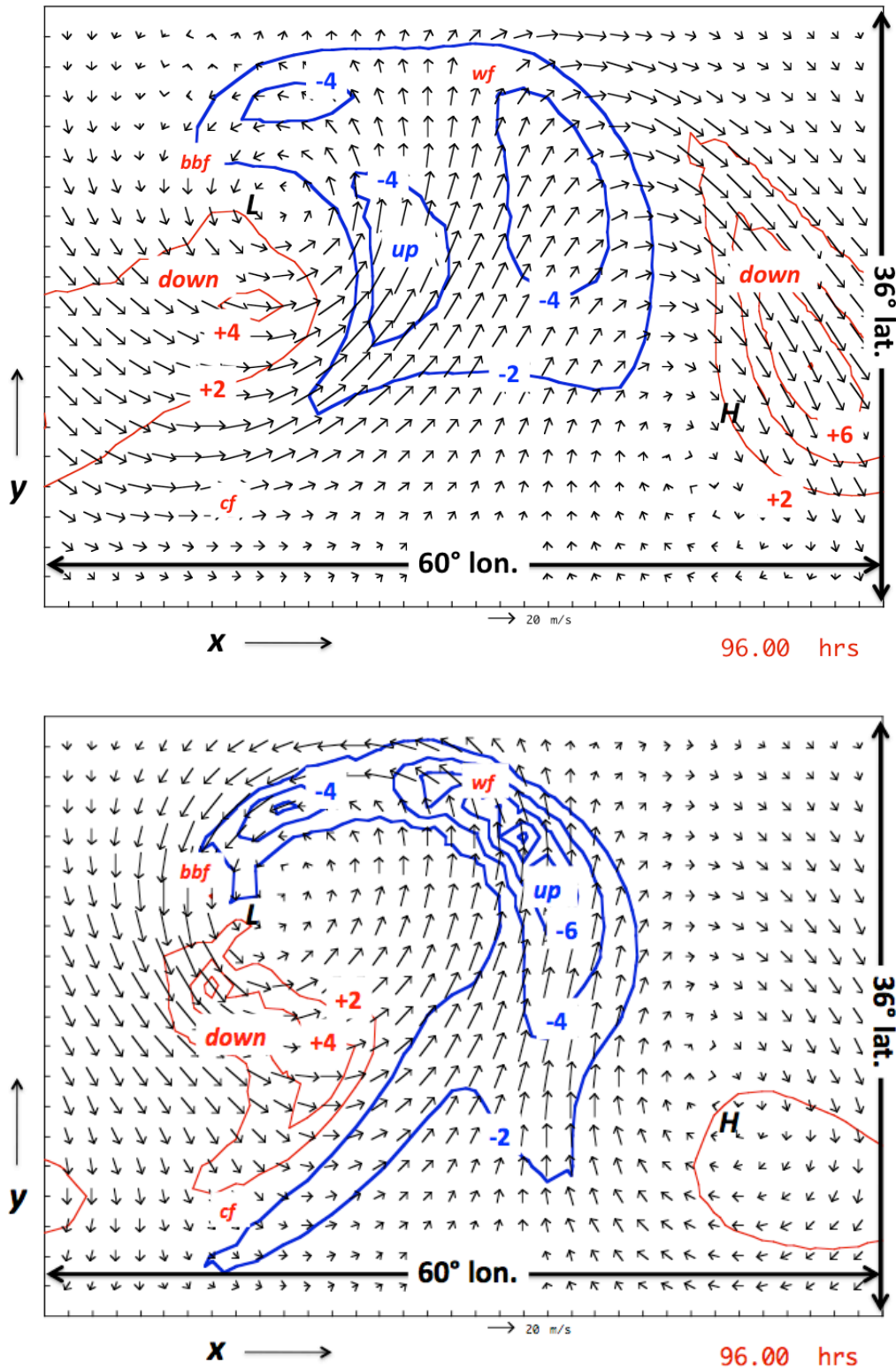
FIGURE 10.15. Isobaric wind vectors and the vertical velocity (labeled in hPa hr^{-1}; **blue: upward motion**; **red: downward motion**; contour interval is 2 hPa hr^{-1}) at t=4 days, at the pressure levels corresponding to p=513 hPa (upper panel) p=865 hPa (lower panel), See **figure 10.7** for further information about the parameter values.
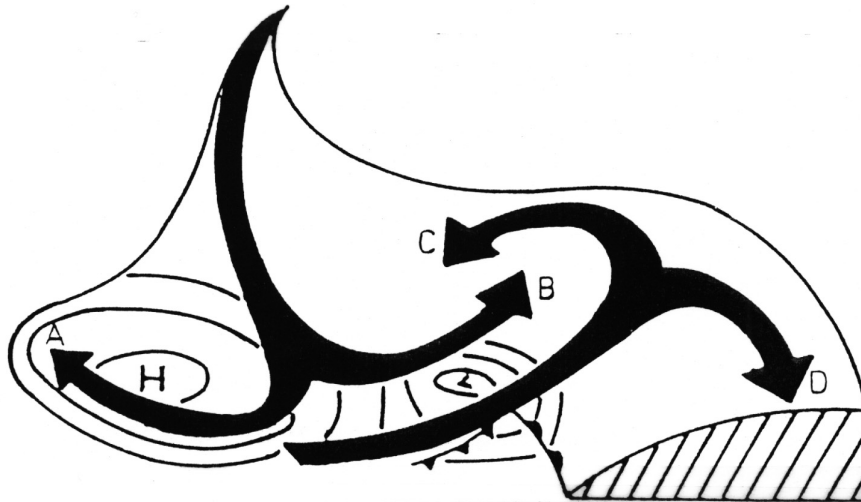
FIGURE 10.16. A schematic of isentropic relative flow within a baroclinic wave. Solid arrows represent flow along a sloping isentropic surface. The surface pressure pattern is indicated (see text for more details) (from Thorncroft, C.D., B.J. Hoskins and M.E. McIntyre, 1993: Two paradigms of baroclinic-wave life-cycle behaviour. **Q.J.R.Meteorol.Soc.**, 119, 17-55).
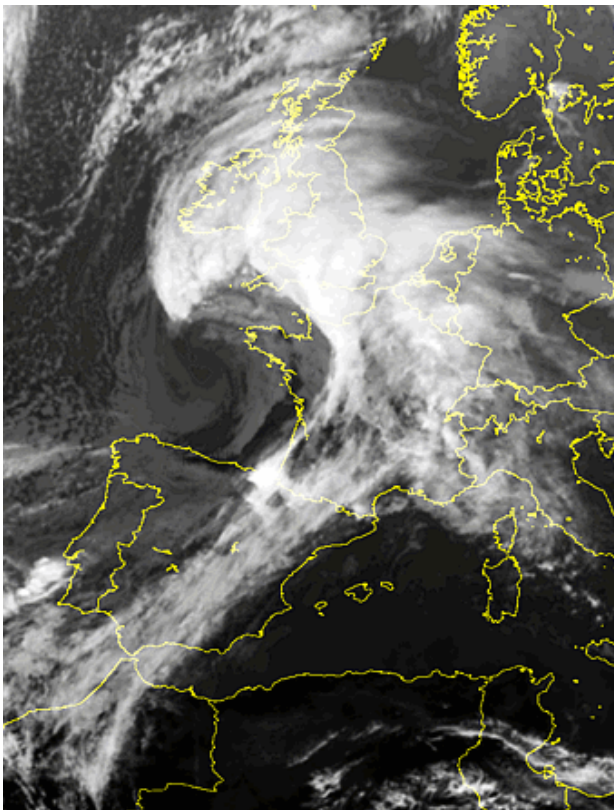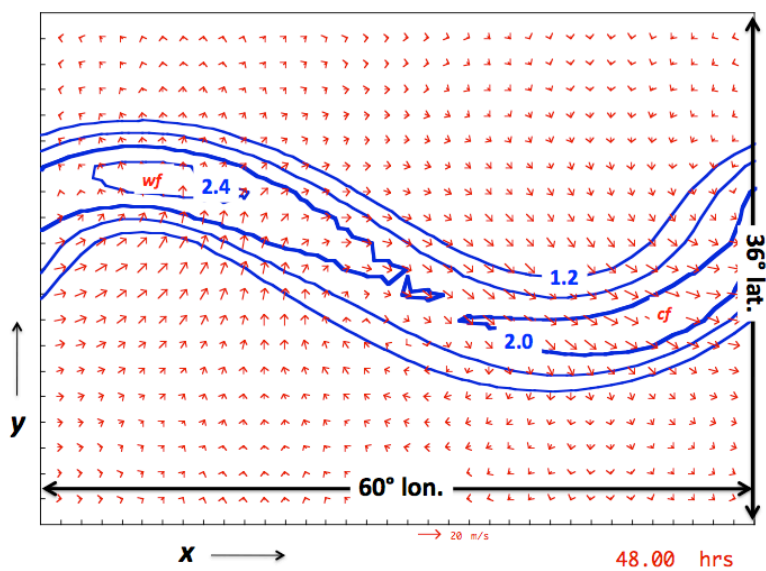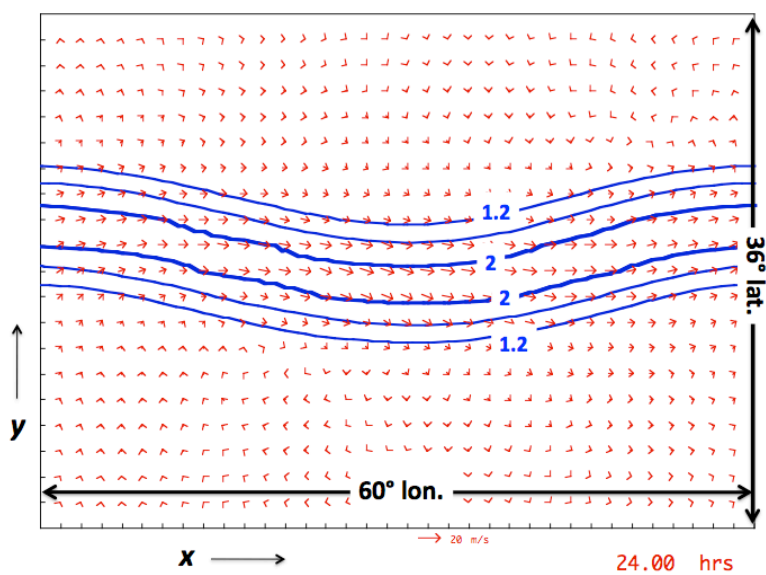

FIGURE 10.17. A cyclone with a cloud pattern that resembles a "hammer-head" (24 November 2012, 14:00 UTC) (MSG infra-red image).

To the extent that condensation occurs in the moist warm sector branch, as it rises, there will be enhanced ascent involving cross-isentropic flow. This pattern of air motion may then result in a cloud pattern with a hammer-head appearance (**figure 10.17**). Since the descending air is certain to be unsaturated, and indeed likely to be very dry, its cyclonic branch B may cut in behind the rising moister air and form a "dry slot" (**figure 9.6**).
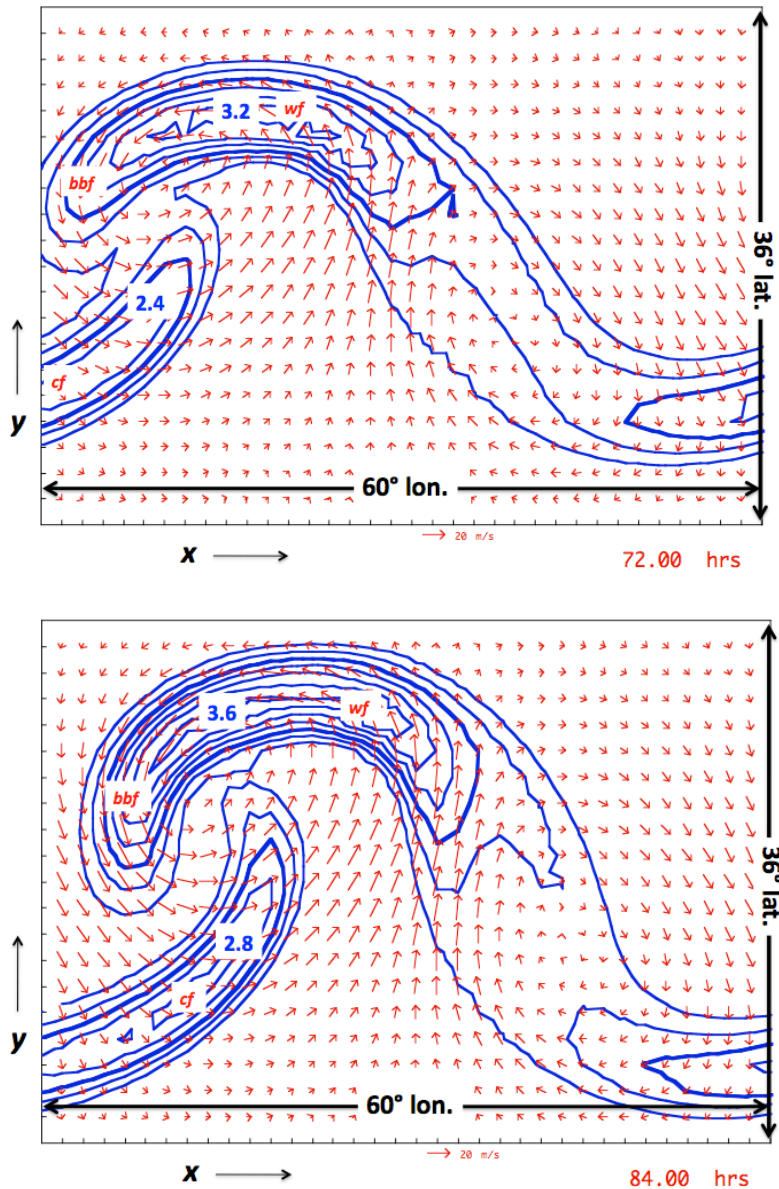
36° lat.

60° lon.

x ⟶

⟶ 20 m/s

24.00 hrs

36° lat.

60° lon.

x ⟶

⟶ 20 m/s

48.00 hrs

36° lat.

60° lon.

x ⟶

⟶ 20 m/s

60.00 hrs
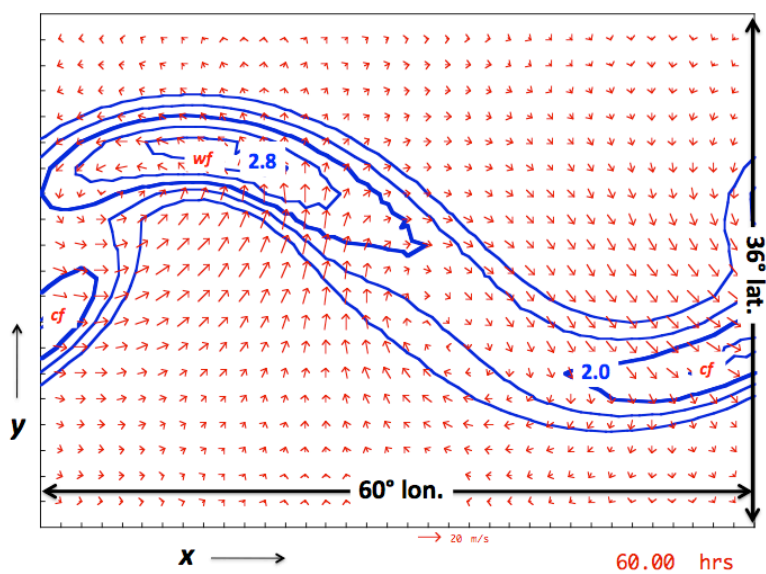
FIGURE 10.18. The flow field (wind vectors) and the absolute value of the temperature gradient (**blue solid lines**; contour interval is $0.4 \cdot 10^{-5}$ K m^{-1}, labels are in units of 10^{-5} K m^{-1}), at different times (indicated in the lower right corner of each figure, for p=865 hPa. The minimum contour-value shown is 1.2×10^{-5} K m^{-1}. The warm front is indicated by "*wf*". The cold front is indicated by "*cf*". The back-bent front is indicated by "*bbf*". See **figure 10.6** for further information about the parameter values. After 72 hours we clearly recognise the "frontal T-bone" of the Shapiro-Keyser conceptual model (**figure 10.3**). The increase of the absolute value of the temperature gradient at 865 hPa is quite spectacular! See the animation of the development of the frontal system at http://www.staff.science.uu.nl/~delde102/BaroclinicLifeCycle.htm

The morphology of the cold front, the warm front and the backbent front and the evolution of these fronts (**figure 10.18**), including the frontal fracture, is very much in accordance with the schematic portrayal given in **figure 10.3**. In fact the simulated middle-latitude unstable baroclinic wave goes through an impressively recognisable life-cycle. Truly remarkable is the increase of the strength of the fronts, i.e. the increase of gradients, in a freely evolving flow, especially after day 2!
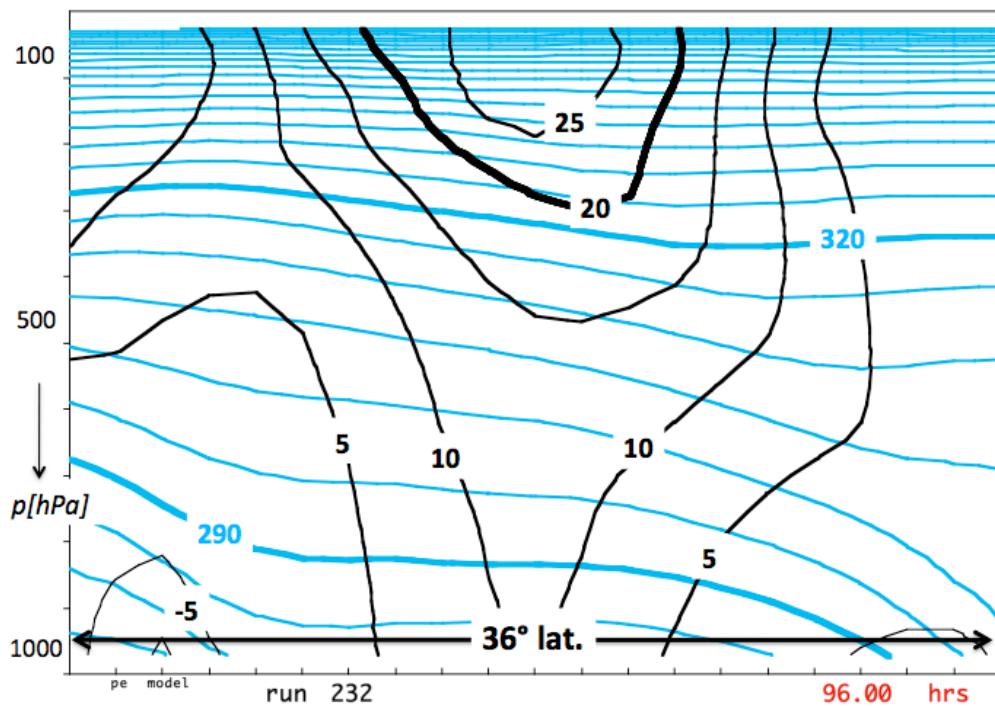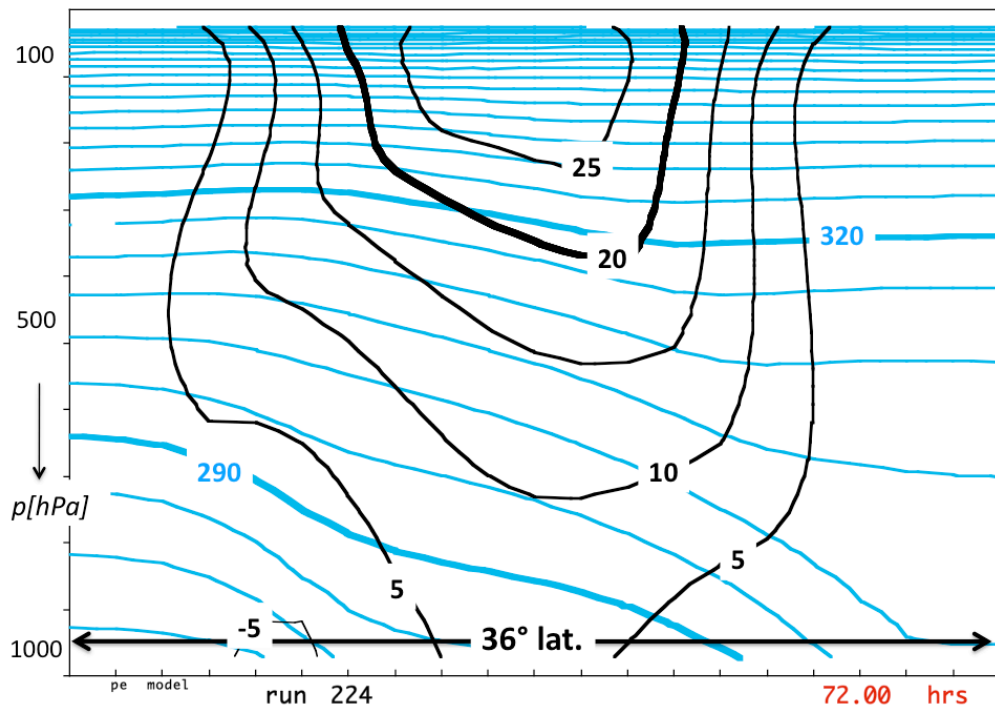
FIGURE 10.19. Meridional cross-section showing the zonal average zonal wind (black contours, labeled in units of m s^{-1}) and the zonal average potential temperature (**cyan**, labeled in units of K) at *t*=3 days (upper panel) and at *t*=4 days (lower panel). The initial state is shown in **figure 10.5**. The *y*-coordinate (latitude) increases towards the right. Note: the increase of the intensity of the surface westerlies, below the jet.

10.8   Wave-mean flow interaction and the Ferrel cell

Figure 10.19 shows meridional cross-sections of the zonal average state at $t=3$ days (upper panel) and at $t=4$ days (lower panel). The initial zonal average state is shown in **figure 10.6**. The meridional flux of heat by the growing baroclinic wave has led to a reduction of the zonally averaged temperature gradient in the "**mixing zone**". At low levels the meridional temperature gradient at the central latitude has been reduced practically to zero. At the surface, eastward winds ($u>0$) have developed in a belt around the central latitude (note: there was no wind at the surface initially). Westward winds ($u<0$) to the north and to the south of this belt are associated with new baroclinic zones (or fronts) that have formed at the southern and northern edges of the "mixing zone". The jet at upper levels has weakened.

Clearly, the zonal mean state of the atmosphere has been altered by the zonal asymmetries, i.e. by the baroclinic wave. In other words, "**wave-mean flow interaction**" has accelerated the zonal mean eastward flow at low levels and decelerated the zonal mean eastward flow at upper levels. If the effect of waves is to decelerate the mean eastward flow, this is referred to as "**planetary wave-drag**" (**chapter 11**).
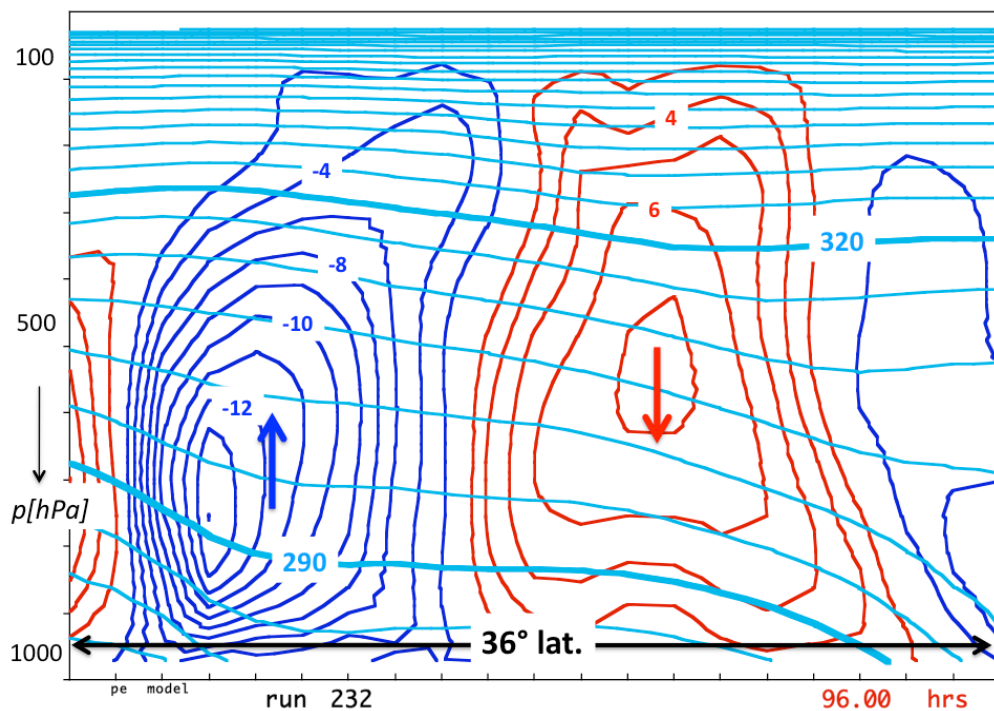

FIGURE 10.20. Meridional cross-section showing the zonal average of the vertical velocity, dp/dt (**blue contours indicate upward motion**; **red contours indicate downward motion**; labeled in units of 0.1 hPa hr^{-1}) and the zonal average of the potential temperature (**cyan**, labeled in units of K) at $t=4$ days in the model. The initial state is shown in **figure 10.5**. The circulation in the eddy-mixing zone in mid-latitudes is called "**Ferrel circulation**". The y-coordinate (latitude) increases towards the right.

Figure 10.20 shows the zonal mean vertical velocity at $t=4$ days. A **thermally indirect zonal mean meridional circulation**, referred to as the "**Ferrel cell**", with upward motion on the cold poleward side and downward motion on the warm equatorward side, is observed. The circulation is closed by poleward *zonal mean* motion at low levels and equatorward *zonal mean* motion at upper levels, which is implicit but not shown in **figure 10.20**. With eastward flow in the northern hemisphere, this yields zonal mean winds blowing from the

south-west at low levels, and zonal mean winds blowing from the north-west at upper levels, in accordance with observations.

William Ferrel and James Thomson[20] attributed the poleward flow at low levels to friction near the Earth's surface, which should lead to a downward decrease of the eastward wind speed, with no attendant decrease of the merdional pressure gradient. As a result, a poleward flow would have to develop, forming the surface branch of an indirect meridional circulation.
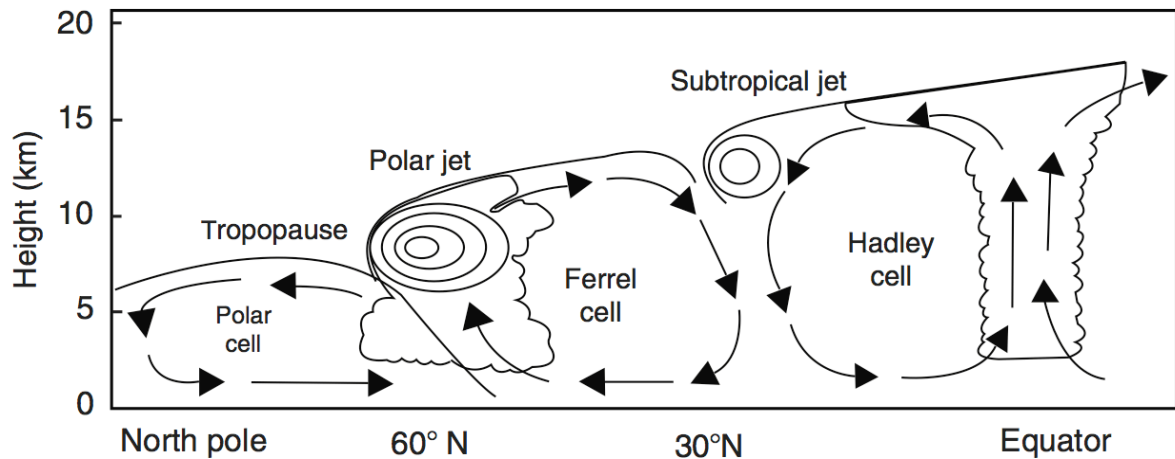

FIGURE 10.21. Traditional schematic view of the principal meridional circulation cells in the troposphere of Earth at equinox, deduced from the velocity distribution. Source: figure 1.15 of K. Mohanakumar: **Stratosphere Tropospher Interactions. An Introduction**. Springer, 2008.

It will be demonstrated in **section 11.5** that the "**Ferrel circulation**" (**figure 10.21**), is a dynamical consequence of the presence of eddies and waves that transport sensible heat and momentum from the tropics to the Pole, or vice-versa. This transport brings the state out of zonal mean thermal wind balance. The Ferrel circulation is required to maintain the zonal mean thermal wind balance, in the same way as a cross-frontal circulation in a frontal region is required to maintain thermal wind balance in the presence of frontogenesis or frontolysis (chapter 9).

10.9   Meridional circulation of mass

We may take a very different viewpoint by plotting the zonal mean meridional mass flux in a cross section with potential temperature as a vertical coordinate, instead of pressure. The total zonal mean instantaneous meridional *isentropic* mass flux is defined as $[v\sigma]$. Here σ is isentropic density, defined in eq. 9 of **Box 7.1**. Square brackets indicate a zonal mean. The unit of mass flux is kg m^{-1} K^{-1} s^{-1}. **Figure 10.22** shows a cross section of $[v\sigma]$ in isentropic coordinates at $t=4$ days, which proves that the total meridional mass flux in the mature stage of the life cycle of an adiabatic unstable baroclinic wave is **poleward in the Middleworld** ($\theta>295$ K in the simulation) and **equatorward in the Underworld** ($\theta<295$ K in the simulation). The poleward mass flux in the Middleworld is directed down the pressure gradient (i.e is upward), while the equatorward mass flux in the Underworld is directed up

---

[20] James Thomson is the older brother of the more famous William Thomson or Lord Kelvin.

the pressure gradient (i.e is downward). This viewpoint, therefore, reveals that, if the influence of zonal asymmetries (eddies and waves) on the meridional mass flux is taken into account, a zonal mean circulation of mass exists, which is opposite in direction to the Ferrel circulation! In fact, cross-isentropic flow is prohibited in this simulation, because of the assumed adiabatic conditions. A real mass-circulation cannot exist in statically sable adiabatic conditions. All motion takes place along isentropes. We are allowed to use potential temperature as a vertical coordinate as long as there is no vertical folding of isentropes, which would immediately render the atmosphere absolutely unstable. In a vertical cross-section with potential temperature as the vertical coordinate, mass is transported only in the horizontal direction, if conditions remain adiabatic. The poleward isentropic mass flux will stop at the end of the adiabatic baroclinic life-cycle.
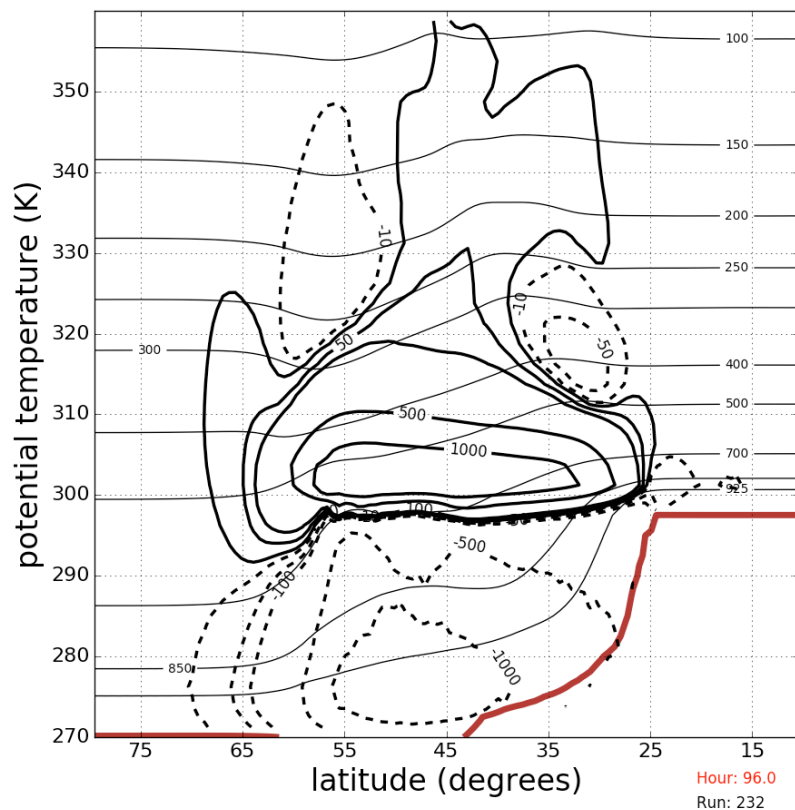

FIGURE 10.22. Zonal mean isentropic mass flux (thick solid and dashed contours), labeled in units of Kg m^{-1}K^{-1}s^{-1}, and pressure (thin contours), labeled in units of hPa, at t=96 hours in the **adiabatic baroclinic life-cycle simulation**. The brown line represents p=1000 hPa, which represents the approximate position of Earth's surface. In this coordinate system adiabatic conditions are revealed by the asbsence of vertical motion, i.e. by the absence of cross-isentropic mass flux. The central latitude, $y=y_0$, corresponds to a latitude of 45°.

In the real atmosphere cross isentropic flow occurs due to either radiative flux divergence or due to latent release. Let us, for simplicity, ignore latent heat release. Diabatic heating (cross-isentropic upwelling) and diabatic cooling (cross-isentropic downwelling), due to radiative flux divergence, operates much like a linear relaxation process, in which the temperature always tends towards a "radiatively determined state"[21]. Therefore, the thermal

[21] The concept of "radiatively determined state" is defined in **sections 2.4 and 12.3**. The Held-Hou model of the Hadley circulation makes use of this concept (**chapter 8**).

effect of radiative flux divergence is frequently simplified by the following equation (see also eq. 8.8).

$$\frac{\partial T}{\partial t} = -\lambda_N \left(T - T_R \right) .$$
(10.61)

T_R represents the temperature of the radiatively determined state, which in many textbooks and scientific publications, is erroneously referred to in this context as the "*radiative equilibrium state*"[22]. The constant of proportionality, λ_N, is called "**Newtonian cooling coefficient**" ($\lambda_N > 0$). The inverse of λ_N is a measure of the time required to adjust to the radiatively determined state, which is very similar to the **radiative equilibrium time scale**, defined in section 2.4. A reasonable estimate for this time scale in the atmosphere is 10-15 days. Here we choose $\lambda_N = 10^{-6}$ s^{-1}, which is associated with a time scale of 11.57 days. The simulation was repeated with this value of λ_N and with T_R identical to the zonal mean temperature distribution at initial time (**figure 10.6**), which implies that the **diabatic process will tend to restore the initial baroclinicity**.
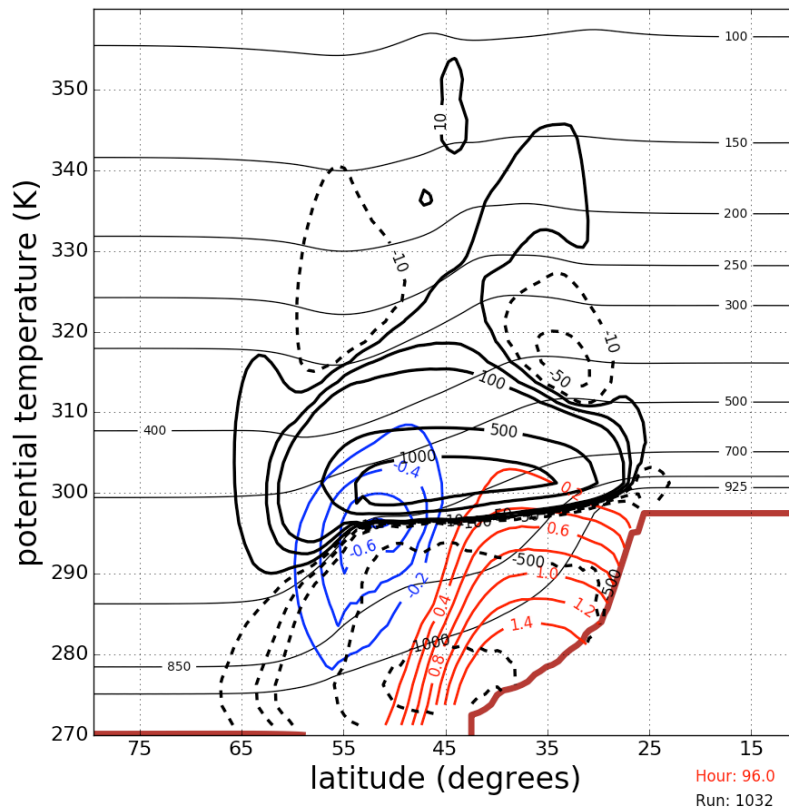

FIGURE 10.23. Zonal mean isentropic mass flux (thick solid and dashed contours), labeled in units of Kg m^{-1}K^{-1}s^{-1}, and pressure (thin contours), labeled in units of hPa, at t=96 hours in the **diabatic baroclinic life-cycle simulation**. The red/blue contours represent isopleths of zonal mean cross-isentropic flow (=[dθ/dt]) , labeled in K day^{-1} (red: **upwelling**; blue: **downwelling**). The brown line represents p=1000 hPa, which coincides with the approximate position of Earth's surface. The central latitude, $y=y_0$, corresponds to a latitude of 45°.

---

[22] Radiatively determined temperature and the radiative equilibrium temperature are usually not distinguished in the scientific literature when a Newtonian cooling parametrisation is introduced (see **chapters 2** and **section 12.3** for an explanation of this distinction).
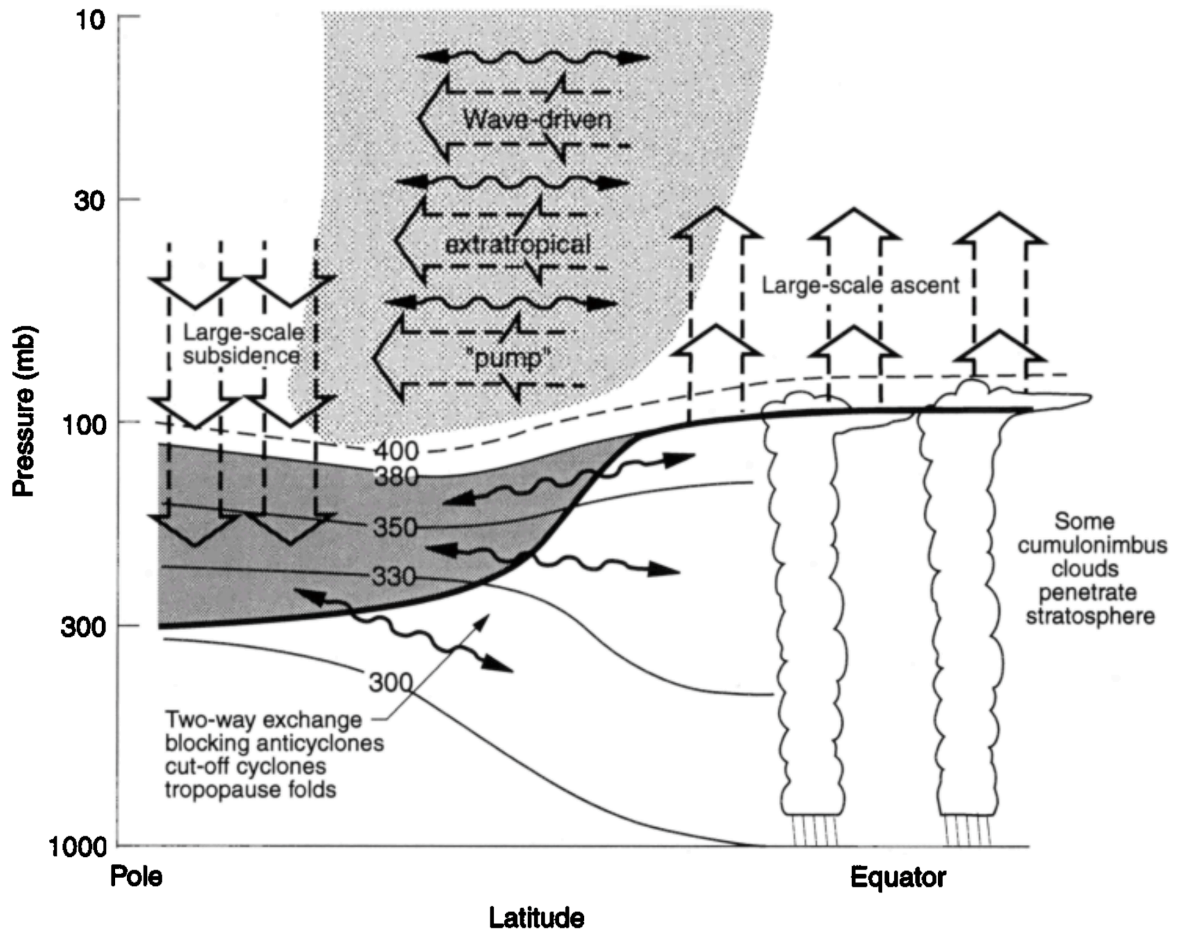
FIGURE 10.24. A popular and schematic view of the four branches of the <u>**long term average Brewer-Dobson circulation**</u> (BDC), according to Holton, et al. (1995). The position of the **dynamical tropopause** is indicated by the thick line. Thin solid lines represent isentropes, labeled in K. The 400 K isentrope is shown as a dashed line. The heavy shaded region is the lowermost stratosphere, which is part of the "Middleworld", or the extra-tropical lower stratosphere, where isentropic surfaces intersect the dynamical tropopause. The region above 380 K is called "Overworld", in which isentropes lie entirely in the stratosphere. Light shading in the Overworld indicates the region of planetary wave-induced "forcing" of an average poleward drift of air, which is sometimes referred to as the "<u>**extra-tropical pump**</u>". The wavy double-headed arrows denote meridional mass-flux by eddy-motions, which represent the meridional component of the BDC. The broad arrows represent cross-isentropic flux by the BDC, which is driven by the extra-tropical pump-mechanism. A mathematical explanation of this mechanism is given in **chapter 11** (see also **section 12.9**). The equatorward flow branch of the BDC (not shown explicitly in this figure) involves equatorward flow of cold polar air in the "Underworld" in "cold-air outbreaks" behind cold fronts, together with cross-isentropic upwelling of this air into the Middleworld. The cross-isentropic branches of the BDC restore atmospheric baroclinicity in middle latitudes. Source: Holton, J.R., et al., 1995: Stratosphere-troposphere exchange. **Reviews of Geophysics, 33**, 403-439.

The adiabatic process, which tends to destroy zonal mean barolinicity, will be counteracted by the diabatic process, which refuels zonal mean baroclinicity by pumping mass from the Middleworld into the Underworld on the poleward side of the baroclinic zone, while pumping mass from the Underworld back into the Middleworld on the equatorward side of the baroclinic zone. This is illustrated in **figure 10.23**, which shows that cross-isentropic downwelling occurs on the poleward side of the central latitude (45°), while cross-isentropic

upwelling occurs on the equatorward side of the central latitude on day 4 of the simulation. Therefore, this diabatic simulation of the life cycle of an unstable baroclinic wave produces a realistic "**diabatic circulation of mass**". Note that the intensity of the **isentropic** component of this mass flux is hardly affected by the **cross-isentropic** mass flux (compare **figures 10.22 and 10.23**).
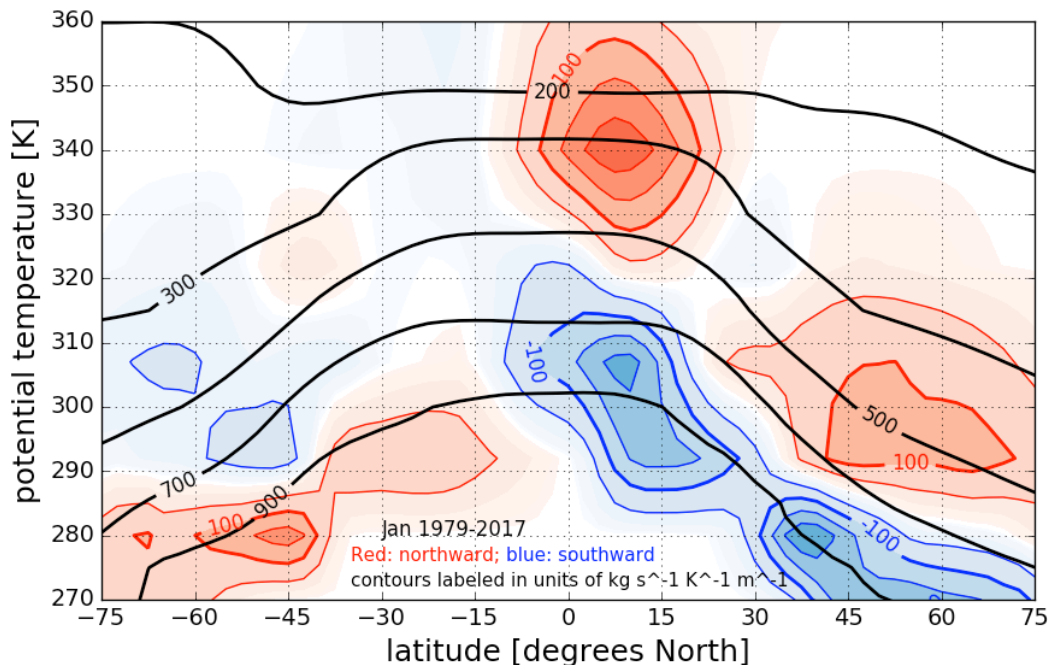

FIGURE 10.25. Monthly mean, zonal mean isentropic mass flux as a function of potential temperature (the vertical coordinate) and latitude for **January** (ensemble average for the years 1979-2017). **Red contours and shading corresponds to a northward mass flux**. **Blue contours and shading corresponds to a southward mass flux**. Contours are drawn at 50 [kg s^{-1} K^{-1} per metre in longitude] intervals. Shading starts at ±5 kg s^{-1} K^{-1} per m in longitude. Black contours represent lines of constant pressure (isobars), labeled in hPa. Deduced from the 6-hourly ERA-Interim reanalysis of pressure and wind on isentropic levels and at the earth's surface (http://apps.ecmwf.int/datasets/). The isentropic mass flux in the middle latitudes, shown in this figure, is an ensemble average over 38 months of January, while the isentropic mass flux, shown in figure 10.23, is instantaneous and representative for the mature, most intense phase, of an unstable baroclinic wave.

Traditionally, the zonal mean meridional atmospheric circulation is divided into three cells (**figure 10.21**). The **Hadley cell, which is driven by radiative and latent heating in the tropics**, is discussed in **chapter 8**. Theoretical reasons are given for its limited latitudinal extent. The indirect meridional circulation cell in middle latitudes, i.e. the "**Ferrel cell**", is "**mechanically forced**" (**section 11.5**), but, as we saw above, the Ferrel circulation does not represent the actual *circulation of mass* in middle latitudes, which is revealed only if mass tranport *by eddies* is included. This mass-circulation has been given the name, "**Brewer-Dobson circulation**", after Alan Brewer and Gordon Dobson, who discovered a systematic poleward stratospheric flux of ozone (Dobson) and of water vapour and Helium (Brewer), from measurements of these constituents in the stratosphere.

A popular portrayal of the Brewer-Dobson mass-circulation, averaged over many baroclinic life cycles is given in **figure 10.24**. This figure gives the impression that most or all the poleward mass flux occurs in the stratosphere. This is not true as is shown in **figure**

10.25. Most of the meridional mass flux occurs in the troposphere in connection with baroclinic waves and has a relatively simple zonal mean pattern, which is very similar to the modelled zonal mean pattern displayed in **figure 10.23**. The most intense zonal mean poleward mass flux in the middle latitudes of the winter hemisphere (in the order of 100 kg s^{-1}K^{-1}m^{-1}) occurs at about 50°N and θ=290-305 K, or in the layer p=400-600 hPa. A zonal mean net *equatorward* mass flux at 50°N is observed *below* θ=285 K (or *below* p=700 hPa). The return-flow of the "Brewer-Dobson circulation", therefore, occurs in a relatively shallow layer. **Figure 10.25** also indicates that the stratospheric part of the poleward branch of "Brewer-Dobson circulation", above 200 hPa, is very weak (<<5 kg s^{-1}K^{-1}m^{-1}).

PROBLEM 10.1. <u>Analysis of a simulation of consecutive baroclinic life-cycles on a large domain</u>

Investigate the output of a simulation of several consecutive life cycles of unstable baroclinic waves on a large domain. Relate the appearance of growing baroclinic waves to frontogenesis, represented by the Q-vector, and the associated pattern of vertical motion. Is this pattern of vertical motion in agreement with the predictions made by the solution of the omega equation (eq. 9.31)? Describe the variations in the intensity of the Ferrel circulation and correlate these variations with the zonal mean *eddy* meridional heat flux. The zonal mean meridional heat flux in pressure coordinates is usually calculated by evaluating

$$\left[v\theta\right] = \left[v\right]\left[\theta\right] + \left[v*\theta*\right]$$

(see section 11.3 for the definition of square bracket and the asterisk). The first term on the r.h.s. of this equation represents the heat flux due to the Ferrel circulation, while the second term represents the eddy heat flux . Can you identify a relation between the first and second term from the output of the simulation? Model data and Python-software will be provided.

PROBLEM 10.2. <u>Analysis of a simulation of a "storm track" by "downstream development"</u>

In reality, the atmosphere is baroclinically unstable in retricted areas, such as on the west side of the Atlantic and Pacific oceans. Wave-like disturbances start growing in these areas, but many times the most intense cyclones develop further downstream in weakly baroclinic regions. This phenomenon, which is known as "downstream development" leads to the formation of a storm track consisting of unstable baroclinic waves in different stages of their development. In this exercise the output of a simulation of such a storm track is provided. Read the paper by Chang (1993) and analyse the dynamics of the simulated storm track in relation to the content of this paper. Model data and Python-software will be provided.

PROBLEM 10.3. <u>The isentropic tropopause</u>

The isentropic tropopause at approximately 30°N, in the layer between θ=330 and θ=370 K is characterised by an intense latitudinal isentropic potential vorticity gradient, which resembles a so-called "PV-step" (chapter 7) (**figure 10.26**). Despite frequent disruptions by waves and eddies, the *time mean* isentropic tropopause remains remarkably sharp and zonally symmetric. How is this possible? Is this due to the zonal symmetry of the isentropic mass flux *convergence* at the poleward edge of the upper outflow leg of the Hadley circulation? Is this due to the zonal symmetry of the cross-isentropic downwelling branch of the Hadley ciculation?   In other words, how zonally symmetric are the upper and downward branches of the Hadley circulation?
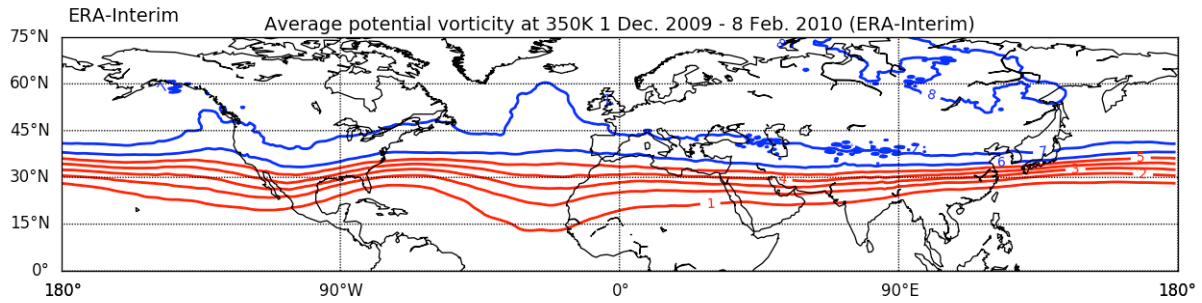
FIGURE 10.26. Time-average distribution of potential vorticity (Z) between 1 December 2009 and 28 February 2010 on the 350 K isentropic surface in the "Middleworld" on the Northern hemisphere, as a function of latitude (°N) and longitude (°E). Red contours correspond to 1, 2, 3, 4 and 5 PVU (tropical air). Blue contours correspond to 6, 7, 8, 9, 10 PVU and higher (extra-tropical air).

The zonal mean isentropic meridional mass flux can be separated into a mean component and an eddy-component as follows:

$$\left[v\sigma\right] = \left[v\right]\left[\sigma\right] + \left[v*\sigma*\right].$$

Similarly, the zonal mean cross-isentropic meridional mass flux can be separated into a mean component and an eddy-component as follows:

$$\left[\frac{d\theta}{dt}\sigma\right] = \left[\frac{d\theta}{dt}\right]\sigma + \left[\left(\frac{d\theta}{dt}\right)^*\sigma*\right]$$

Investigate the above questions by comparing the mean isentropic mass flux and eddy isentropic mass flux at $\theta=340$ K and by comparing the mean cross-isentropic mass flux and eddy cross-isentropic mass flux at $\theta=340$ K (**figure 10.25**). Data and sript will be provided.

ABSTRACT OF CHAPTER 10

Chapter 10 describes the structure of the **dynamical core** of a hydrostatic numerical **primitive equation model** of the atmospheric circulation. These models use $\sigma=p/p_s$ as a vertical coordinate (**sigma-coordinate**). This avoids problems with imposing upper and lower boundary conditions.

A sigma coordinate hydrostatic model is used to simulate the life cycle of an unstable baroclinic wave. This is done for highly idealised conditions, neglecting the effect of the curvature of the Earth's surface (f is constant) and assuming adiabatic conditions, which implies that air parcels cannot cross isentropes. Despite these idealisations, the modeled life cycle of an unstable baroclinic wave, starting from an west-east oriented front and associated jet, is remarkably realistic. The formation of a cyclone with **a warm front, a cold front and a back-bent front, including the frontal fracture** during the mature stage of the life cycle, after 4 days, are reproduced by the model exactly as portrayed by the conceptual model, which was proposed by the Bergen School in the 1920's and by Shapiro and Keyser in 1990.

The qualitative predictions made by the **omega equation** (chapter 9), about the pattern of vertical motion within a baroclinic wave, are verified by the simulation, i.e upward motion

occurs east of the upper level trough, while downward motion (subsidence) occurs west of the upper level trough.

An important action of middle latitude baroclinic waves and eddies is to **transport heat in the poleward direction** and thus to reduce the zonal mean meridional temperature gradient as well as the associated vertical shear of the zonal wind. According to quasi-geostrophic theory this requires a **zonal mean meridional indirect circulation** with upward motion on the cold (poleward) side and downward motion on the warm (equatorward) side. This circulation is named "**Ferrel circulation**", in honour of William Ferrel, one of the founding fathers of modern dynamical meteorology.

The apparent inconsistency between the indirect Ferrel circulation and the **direct Brewer-Dobson circulation** is illustrated and reconciled. This issue is addressed further in chapters 11 and 12.

Further reading

Books

Coiffier, J., 2009: **Fundamentals of Numerical Weather Prediction**. Cambridge University Press, 340 pp. (A rather technical book about the structure of numerical models for weather prediction)

Durran, D.L., 2010: **Numerical Methods for Fluid Dynamics**. Springer Texts in Applied Mathematics, vol 32. 527 pp. (Balanced overview of numerical methods in fluid dynamics, focusing on atmosphere)

Haltiner, G.J., and R.T. Williams, 1980: **Numerical Prediction and Dynamic Meteorology.** Second edition. John Wiley & Sons. 477 pp, p. 397. (Second edition of a classic on Dynamic Meteorology that was written in the 1950's)

Warner, T.T., 2011: **Numerical Weather and Climate Prediction**. Cambridge University Press, 526 pp. (An up to date account of all aspects of numerical modeling in meteorology).

Washington, W.M., and C.L. Parkinson, 1986: **An Introduction to Three-dimensional Climate Modeling.** Oxford University Press. 422 pp. (Warren Washington stood at the dawn of climate modelling at NCAR. The first edition has been replaced by second edition in 2005)

Articles

Chang,, E.K.M., 1993: Downstream development of baroclinic waves as inferred from regression analysis. **J.Atmos.Sci., 50**, 2038-2053

Davies, H.C., Ch. Schär and H. Wernli, 1991: The palette of fronts and cyclones within a baroclinic wave development. **J.Atmos.Sci., 48**, 1666-1689. (One of series of papers illustrating the role of barotropic shear in the morphology of fronts accompanying the life cycle of an unstable baroclinic wave)

Hoskins, B.J., 1983: Dynamical processes in the atmosphere and the use of models. **Q.J.R.Meteorol.Soc.**, **109**, 1-21.

Mudrick, S.E., 1974: A numerical study of frontogenesis. **J.Atmos.Sci., 31**, 869-892. (the first high resolution *primitive equation* model simulation of the life cycle of an unstable baroclinic wave showing the formation of the warm front, cold front and back-bent front including the frontal fracture)

Thorncroft, C.D., B.J. Hoskins and M.E. McIntyre, 1993: Two paradigms of baroclinic-wave life-cycle behaviour. **Q.J.R.Meteorol.Soc.**, **119**, 17-55. (This paper focuses on the later stages of different baroclinic life cycles, showing that barotropic shear plays an important role in determining the "breaking" of these waves and the appearance of "cut-off lows and highs")

Williamson, D.L., 2007: The evolution of dynamical cores for global atmospheric models. **J.Meteorol.Soc.Japan, 85B**, 241-269. (An informative general review of the development of numerical models of the atmosphere, in particular of the dynamical core, with a discussion of the "pole problem")

Websites

http://www.staff.science.uu.nl/~delde102/BaroclinicLifeCycle.htm
http://www.staff.science.uu.nl/~delde102/AtmosphericDynamics.htm

List of problems (chapter 10)